Design and Testing of a Terahertz Bandstop Filter Using Varying Radii Split-Ring Resonators

by

Saeid Asadi

B.Sc., Islamic Azad University of Kermanshah, 2008

M.Sc., University of Sistan and Baluchestan, 2013

A Thesis Submitted in Partial Fulfillment of the Requirements for the Degree of

Master of Applied Science

In the Department of Electrical and Computer Engineering

We acknowledge and respect the Lək̓ʷəŋən (Songhees and Esquimalt) Peoples on whose territory the university stands, and the Lək̓ʷəŋən and W̱SÁNEĆ Peoples whose historical relationships with the land continue to this day.

Design and Testing of a Terahertz Bandstop Filter Using Varying Radii Split-Ring Resonators

by

Saeid Asadi

B.Sc., Islamic Azad University of Kermanshah, 2008

M.Sc., University of Sistan and Baluchestan, 2013

Supervisory Committee

Dr. Thomas Darcie, Co-supervisor
(Department of Electrical and Computer Engineering)

Dr. Levi Smith, Co-supervisor
(Department of Electrical and Computer Engineering)

Abstract

The terahertz (THz) band which ranges from 0.1 THz to 10 THz has been relatively unexplored when compared to other frequency bands due to the unavailability of sources and detectors. However, continual advances in technology have made this frequency band more accessible and have attracted attention because of unique applications such as imaging, spectroscopy, communications, and physical defect detection. In many applications throughout the electromagnetic spectrum signal filtering is used to improve signal-to-noise ratios. One method to filter signals is using split-ring resonators (SRRs) that are made of nonmagnetic metals which respond to electromagnetic waves like a magnetic medium. SRRs at their resonant frequency create a magnetic dipole so that they can stop or pass electromagnetic waves. This property has made SRRs a commonplace element in the design of metamaterials (MTMs). This thesis does not focus on the investigation of MTM properties and characteristics (negative permittivity or negative permeability), but it does provide some of the relevant background and theory.

This thesis reports a proof-of-concept terahertz band-stop filter constructed from SRRs that has a center frequency of 1.06 THz and a -3 dB bandwidth of 0.36 THz. The design consists of nine SRRs of varying radii (3×13 μm, 3×14 μm, 3×15 μm) that are placed between the conductors of a coplanar stripline (CPS). The response of the filter is measured using a modified terahertz time-domain spectrometer and a reasonable agreement between simulation and experiment was found. This work demonstrates the viability of using varying-radii SRRs as discrete sub-wavelength filter elements for THz systems. In addition, the ABCD matrix approach was utilized to get the transmission response of the equivalent circuit. This filter was fabricated using gold on a thin Si_3N_4 substrate, and the simulated data are in good agreement with the experimental results.

Contents

Tables

Figures

Acronyms

CSRR	Complimentary Split-Ring Resonator
CPS	Coplanar Stripline
CPW	Coplanar Waveguide
EM	Electromagnetic
FWHM	Full Wave at Half Maximum
GHz	Gigahertz
LH	Left-Handed
LTG-GaAs	Low Temperature Grown Gallium Arsenide
MTM	Metamaterial
PCS	Photoconductive Switch
Rx	Receiver
SRR	Split-Ring Resonator
THz	Terahertz
THz-TDS	Terahertz Time Domain Spectroscopy
TL	Transmission Line
Tx	Transmitter

Acknowledgements

I am grateful to Prof. Darcie and Dr. Smith for giving me the opportunity to continue my education at the University of Victoria and conduct THz research in their lab. Due to this opportunity, I gained valuable experience, learned new skills, and deepened my understanding. I appreciate their invaluable guidance, support, and constructive feedback. Beyond academic growth, studying at UVic and living in Victoria have provided me with invaluable life lessons.

I would like to thank my friends in the THz group: Mohsen Haghighat and Ali Dehghanian for fabricating photoconductive switches and helping me with my courses. I also thank my lab colleague, Behnam Khosravi, and my friend Arman Goudarzi for their help with my courses. I am grateful to all my friends at UVic and in Victoria for the happy times we shared. Last but not least, I thank my family for their unwavering help and support.

Research Objectives and Organization of Thesis

Filtering is used for manipulating signals and is widely used in electronics and optics to reject or pass desired frequency bands. This need for filters continues to exist within the terahertz (THz) range, which resides between the electronic and optical domains. One method to filter THz signals is using split-ring resonators (SRRs) which have several benefits: first, the size of SRRs is small, so that SRRs can be inserted easily in the circuit along with transmission lines. Second, SRRs are coupled to the electromagnetic waves magnetically (inductively) or electrically (capacitively) without a connection to the transmission line. For this, there is no need for series or shunt stubs. The main objective of this thesis is to design a wide-bandstop filter by loading a coplanar stripline (CPS) with SRRs. In addition to the main objective, the investigation of prototype bandpass filters with SRRs and rectangular rods were simulated as other goals. Regarding the structure of this thesis, the organization is as follows:

- Chapter 1 provides introductory information about THz waves and applications, the CPS, the SSR and a literature review of filters based on transmission lines loaded with SRRs.
- Chapter 2 discusses the theory of SRRs, and the equivalent circuit model of transmission lines loaded with SRRs.
- Chapter 3 provides the results including simulations, experiments, the equivalent circuit model for the structure, extraction of parameters of the circuit model, and ABCD matrix method.
- Chapter 4 is dedicated to contributions.
- Chapter 5 is where the conclusion and future work are presented.
- Appendices:
    - Appendix A is about generation and detection of THz waves and time-domain THz spectroscopy.
    - Appendix B provides information for ABCD matrix approach.

Chapter 1

Introduction

This chapter contains general information about terahertz (THz) waves and applications, coplanar stripline (CPS), split-ring resonators (SRR), and CPS loaded with SRRs for filtering. A literature review concerning filters with SRRs-loaded transmission lines is provided.

1.1 Terahertz wave and applications

The THz region of the electromagnetic spectrum (0.1×10^{12} Hz to 10×10^{12} Hz) is depicted in Fig. 1.1. It lies between the microwave and far infrared regions and has garnered significant attention owing to its properties and applications in different scientific and technological domains. THz waves are not visible to naked eyes. The energy of THz waves is low, for instance 4.14 meV @ 1 THz. Due to the low photon energy of THz waves, the presence of thermal noise makes it difficult to detect THz signals at room-temperature. And also owing to the frequency operation limitations of solid-state electronic components, such as oscillators and amplifiers, at THz frequencies, the terahertz spectrum has not been investigated sufficiently [1].

The low photon energy of electromagnetic waves at THz frequencies makes this band safe when compared to photon energies of X-rays which are ionizing [2]. Another important characteristic of THz waves is the capability to penetrate through some materials which enables non-invasive medical imaging and diagnostics [3] and security screening [4]. THz waves are well suited to spectroscopy, biomedical research [5] and material characterization [6] because they can excite low-frequency molecular vibrations. Lastly, the ability of high-data-rate communication due to the wide bandwidth of THz signals makes them suitable for the next generation of communications [7]. Due to technological advancements such as fiber-based femtosecond lasers, the generation and detection of THz electromagnetic waves has become more accessible [8]. With the growth of THz technology, the need for THz devices, such as absorbers, filters, modulators, and so on, is increasing [9]. Generation and detection of THz electromagnetic waves are discussed in Appendix A.

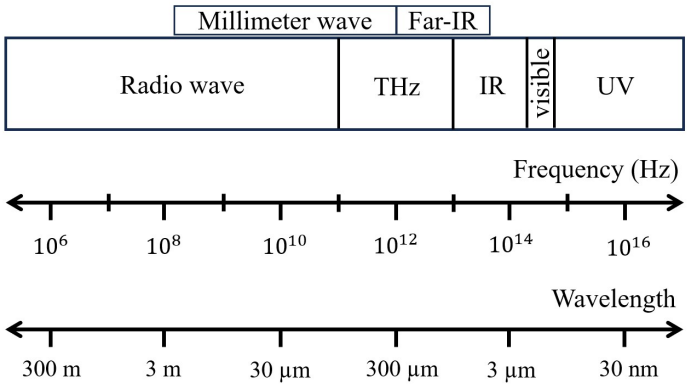

Fig. 1.1. THz spectrum. Frequency, wavelength, and energy of THz band are illustrated [2].

1.2 Coplanar stripline

There are many types of transmission lines that are capable of transmitting signals between different ports of circuits. As some examples of transmission lines, Fig. 1.2 shows coaxial and two-wire lines, and in Fig. 1.3, four types of planar transmission lines are represented.

Depending on the specific application, one of the transmission lines is generally preferred. In the design and experiments done in this thesis, the coplanar stripline (CPS) is chosen owing to its desirable attenuations and dispersion characteristics. A CPS is a structure containing of two uniplanar strip transmission lines on the same dielectric as shown in Fig. 1.3(b). In this figure, W, S, and t are width of each CPS, separation between coplanar striplines, and thickness of CPS, respectively, and h is the height of the substrate with a dielectric permittivity of ϵ_r[10].

CPS possesses appealing characteristics including the straightforward integration of shunt and series passive or active components, eliminating the necessity for vias to establish connections with the ground plane which is necessary for microstrip topologies [11]. Additionally, the balanced CPS mode is straightforward to excite [12] and is used for applications such as balanced mixers [13] and dipole antenna arrays [14]. In addition to these properties, when CPS is fabricated on a thin membrane as its substrate, CPS exhibits low attenuation and dispersion at THz frequencies, which are elaborated on in the following paragraphs.

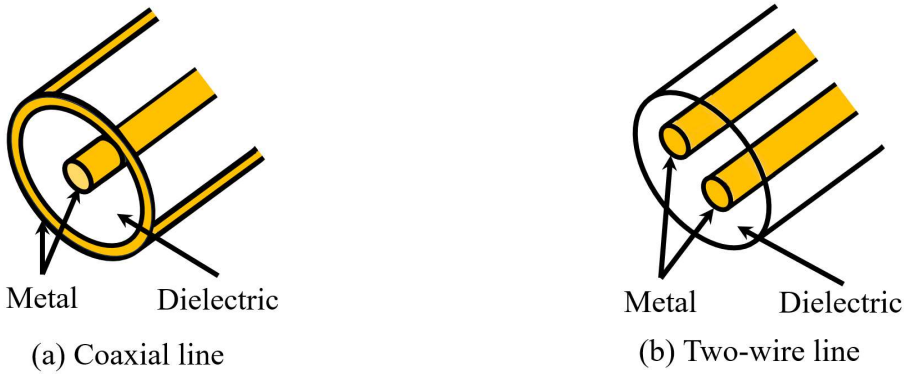

Fig. 1.2. (a) coaxial transmission line. (b) two-wire transmission line [15].

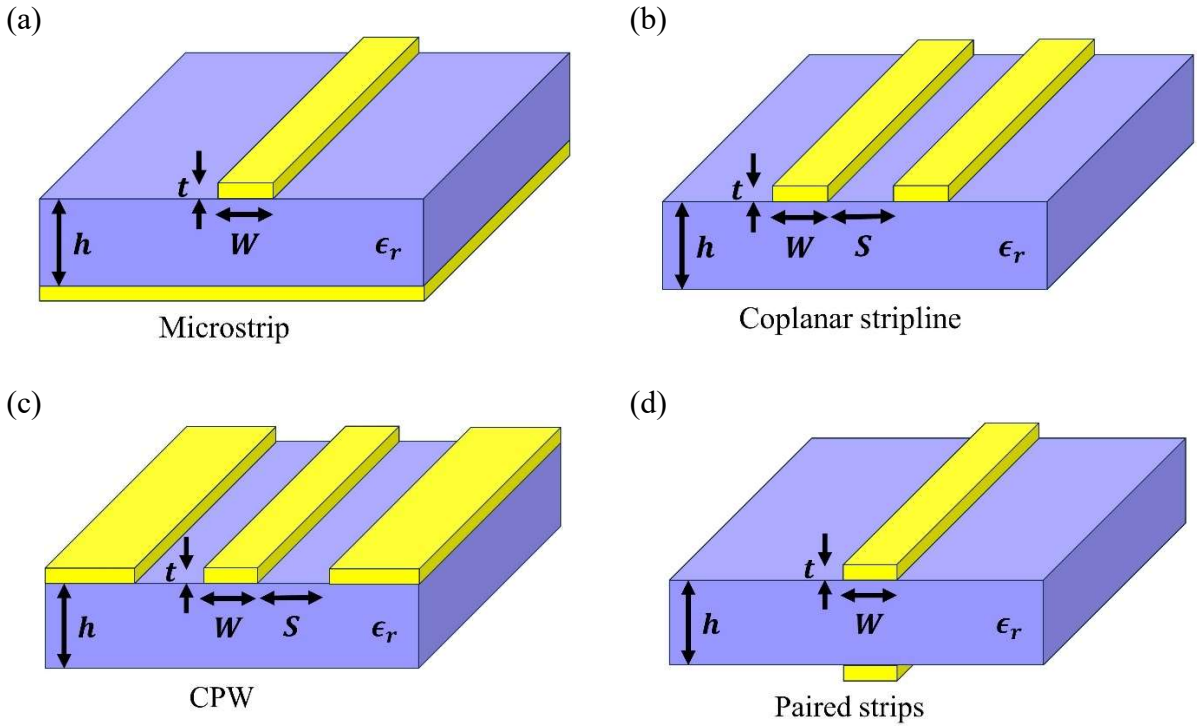

Fig. 1.3. Four type of planar transmission lines fabricated on a substrate with dielectric constant ϵ_r. (a) Microstrip, (b) coplanar strip lines, (c) coplanar waveguides, and (d) paired-strip lines [10].

1.2.1 Attenuation in coplanar striplines

When electromagnetic waves propagate along a transmission line the losses reduce the amplitude of the wave (or pulse amplitude). To illustrate this phenomenon, Fig. 1.4 plots a sub-picosecond

pulse which contains frequency components that extend into the THz region along a standard CPS with a thick (relative to the wavelength) substrate. As it is seen, the amplitude of the original pulse decreases dramatically [16]. For thick substrates, the wave propagation to the substrate is the dominant loss mechanism, and it is caused by a mismatch between the transmission line permittivity and substrate permittivity. Indeed, due to this mismatch in permittivity, the guided wave above the substrate propagates faster than the propagated wave inside the substrate. For this, the guided wave propagates energy into the substrate at the radiation angle of ψ [16], [17], which is shown in Fig. 1.5.

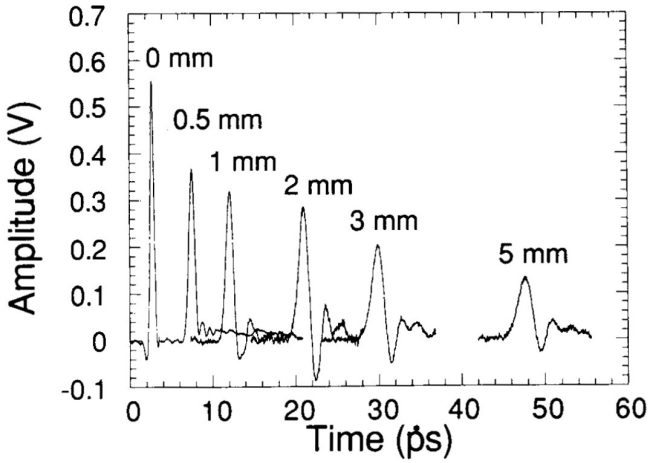

Fig. 1.4. Data of propagation of a typical pico-second pulse, in time, over coplanar transmission lines on a bulk substrate. The distance that the pulse has propagated is shown in millimetre 'mm' [16] © [1991] IEEE.

Equation (1. 1) explains how the radiation angle of shock waves is defined. In this formula, k_z, k_d, ϵ_{eff}, and ϵ_{r} are propagation constant along the CPS, propagation constant of the shock wave, effective permittivity seen by the guided wave, and dielectric permittivity seen by the shock wave, respectively [16].

$$\cos(\psi) = \frac{k_z}{k_d} = \frac{\sqrt{\epsilon_{\text{eff}}(f)}}{\sqrt{\epsilon_r}} \tag{1. 1}$$

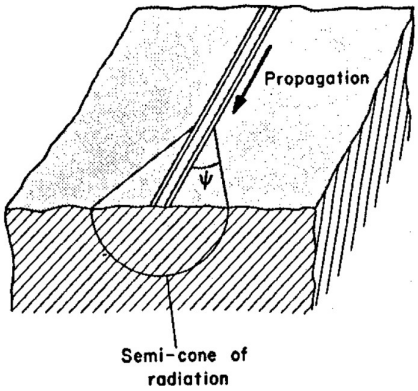

Fig. 1.5. Propagation of the shock wave from CPS in to the substrate with angle ψ [17] © [1983] IEEE.

Ohmic loss is the other source of attenuation of waves. The surface resistance concept is a convenient way to calculate ohmic loss of CPS. The surface resistance is the real part of the intrinsic impedance (η) of a conductor, formula (1. 2). Where, ω, μ, σ_c, and j are angular frequency, permeability of the transmission line, conductivity of the transmission line, and imaginary unit, respectively [18].

$$R_s = Re\{\eta\} = Re\left\{(1+j)\sqrt{\frac{\omega\mu}{2\sigma_c}}\right\} \tag{1. 2}$$

In addition to the shock wave and ohmic loss, dielectric loss, which is divided to (a) conduction loss in the dielectric and (b) dielectric damping, is the other source of attenuation. The conduction loss is because of the movement of carrier charges inside the dielectric which is proportional to the conductivity of the dielectric, σ_d. And the dielectric damping is owing to vibration of the lattice, inside the dielectric, originating from an electric field inside the dielectric. With increasing frequency, the dielectric damping increases [19].

An effective technique to address losses in CPS is using a structure to decrease the mismatch between ϵ_{eff} and ϵ_{r}. In this regard, reducing the thickness of the substrate and using a dielectric with a permittivity close to the permittivity of the air is a promising approach which is done in [20], and the results are provided in Fig. 1.6. As it is seen in this figure, the coplanar transmission line fabricated on a thin membrane shows negligible attenuation which is mostly due to the ohmic loss of the coplanar transmission line.

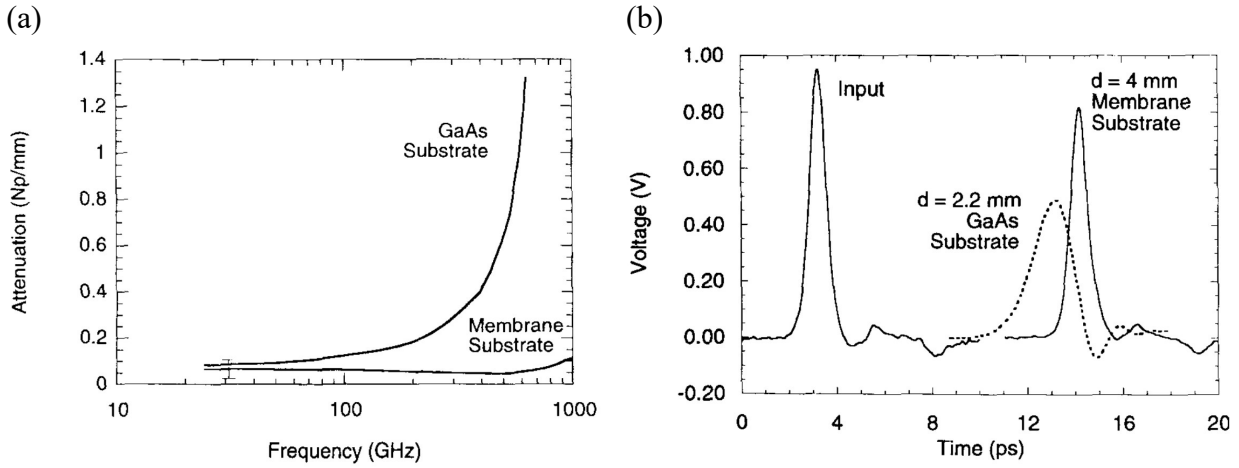

Fig. 1.6. Attenuation of THz bandpass pulses propagating on CPS fabricated on a thin membrane and a bulk GaAs. (a) Attenuation in the frequency domain. (b) Propagation of a pico-second pulses (THz bandpass) on CPS [20] © [1994] IEEE.

1.2.2 Dispersion in coplanar striplines

In a dispersive transmission line, different frequencies travel at different speeds. As a result, different frequency components of a signal do not travel together which causes a pulse to broaden. This phenomenon is named *dispersion*, and may cause difficulties in gaining information from transmitted signals [19]. In a dispersive medium, the phase and group velocities are not constant with respect to frequency. In Fig. 1.4, the pulse broadening associated with the dispersion of a typical sub-picosecond pulse is illustrated.

Decreasing the thickness of the substrate results in a decrease in the radiative loss and dispersion. Considering Fig. 1.6(b), the sub-picosecond pulse propagating on CPS with a thin substrate, after 4 mm, has a little pulse broadening when compared to a thick GaAs substrate over half distance. Fig. 1.7 shows the phase velocity of a THz bandpass pulse propagating on the same CPS, fabricated on a GaAs substrate and a thin membrane. As it is seen, the phase velocity ($v_p \approx 0.9c$) of the pulse with thin membrane is relatively independent of frequency. Whereas the thick GaAs substrate exhibits a stronger frequency dependence [20].

Therefore, utilising a thin membrane as a substrate for coplanar striplines not only results in lower attenuation, but also the dispersion of the propagating pulse is very small. In all the experiments performed in this thesis, a thin Si_3N_4 membrane is used for these benefits.

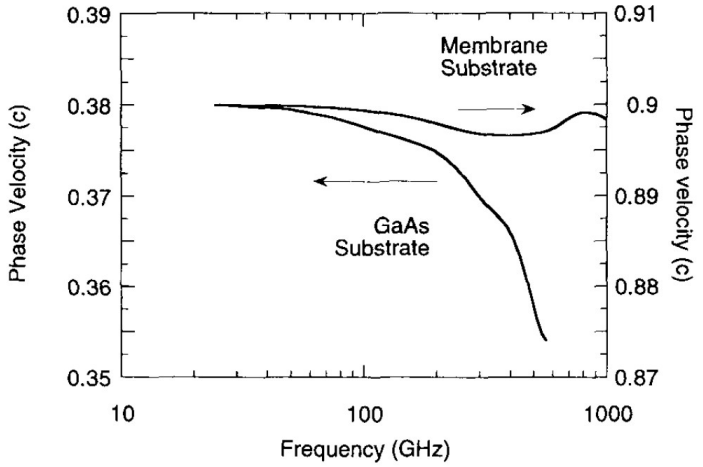

Fig. 1.7. Phase velocity of a THz bandpass pulse on the same CPS over substrates of GaAs and thin membrane. The vertical axis is normalized based on speed of light in the air [20] © [1994] IEEE.

1.3 Filters

Applications and requirements of electrical or optical systems dictate which frequency or frequency band should be utilized. For this, there is a need to reject or pass specific frequencies since the presence of unwanted frequency components may cause distortion or system performance degradation. For example, the nonlinear effect of components creates harmonics which these harmonics could lie in the desirable frequency band, and as a result, leads to a distortion of the desirable signals. Filters play the role of passing and or suppressing signal frequencies.

Regarding desirable frequencies in THz band, some cases are as follows: carrier frequencies in communications could be from 100 GHz to 625 GHz [7]. In spectroscopy, different THz frequencies are used such as 717 GHz for measuring aqueous DNA molecules [21], or 1–15 THz range for detecting amino acids [22]. In THz imaging, tryptophan concentration is a biomarker for skin cancer detection. The resonance absorption modes of tryptophan are at 1.42 THz and 1.84 THz. [23]. Considering these applications, there is a need to use filters to pass and or stop frequency components (or a frequency range) in THz systems.

There are four common filter types: low-pass, high-pass, bandpass, and bandstop which are explained briefly in the subsequent paragraphs.

1.3.1 Low-pass filters

In low pass filters, the passband starts from DC to a desired cutoff frequency (-3 dB attenuation). Over the passband, there is a low attenuation, but out of the passband, the signal is attenuated.

Fig. 1.8 illustrates a general configuration of low-pass filters with the frequency response. Capacitors behave like short and open circuits in high and low frequencies, respectively. Conversely, inductors behave like open and short circuits in high and low frequencies, respectively. In this figure, the cutoff frequency is marked by f_c. Before this frequency, the attenuation is negligible, but after this frequency the attenuation is large.

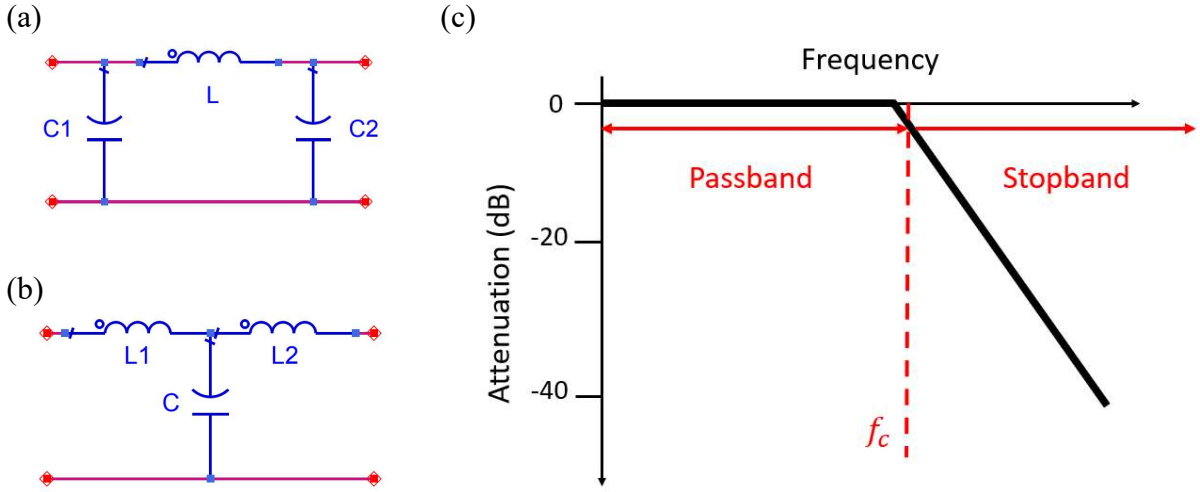

Fig. 1.8. A Low-pass filter. (a) Pi model. (b) T model. (c) Frequency response [24].

1.3.2 High-pass filters

High-pass filters are the opposite of low-pass filters. High-pass filters pass frequency components higher than a desired frequency (cutoff frequency) with negligible attenuation and attenuate frequency components lower than the cutoff frequency. In Fig. 1.9, simple structures of high-pass filters with the frequency response are shown. The cutoff frequency is commented by f_c.

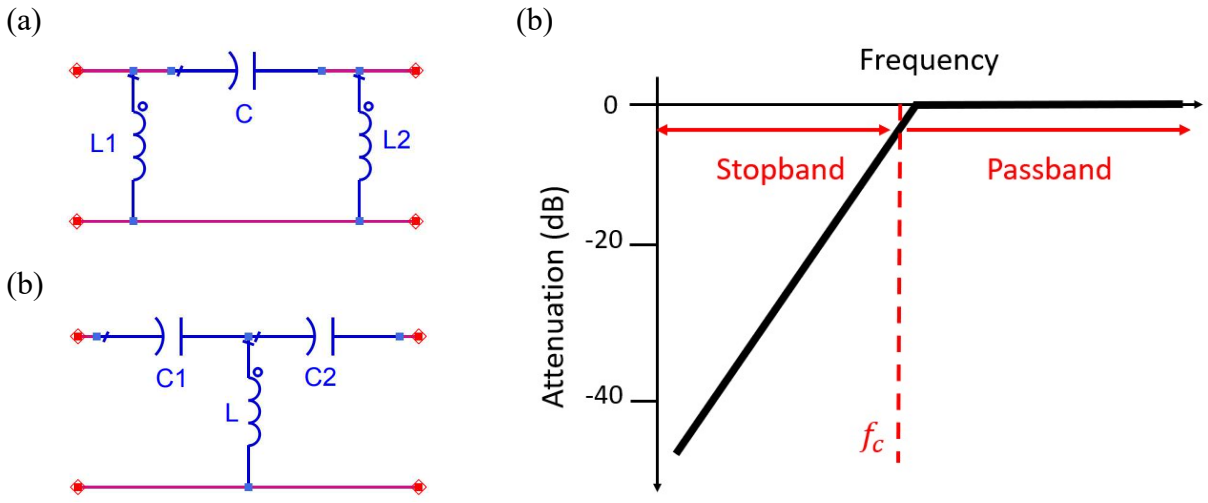

Fig. 1.9. A high-pass filter. (a) pi model. (b) T model. (c) frequency response [24].

1.3.3 Bandpass filters

Band-pass filters have passbands limited by a lower and an upper cutoff frequency so that frequency components between these two cutoff frequencies pass from the filter with a minimum attenuation, but frequencies out of passband are attenuated strongly. Fig. 1.10 illustrates a passband filter with pi and T models and the general frequency response. f_{cl} and f_{ch} are the lower and upper cutoff frequencies.

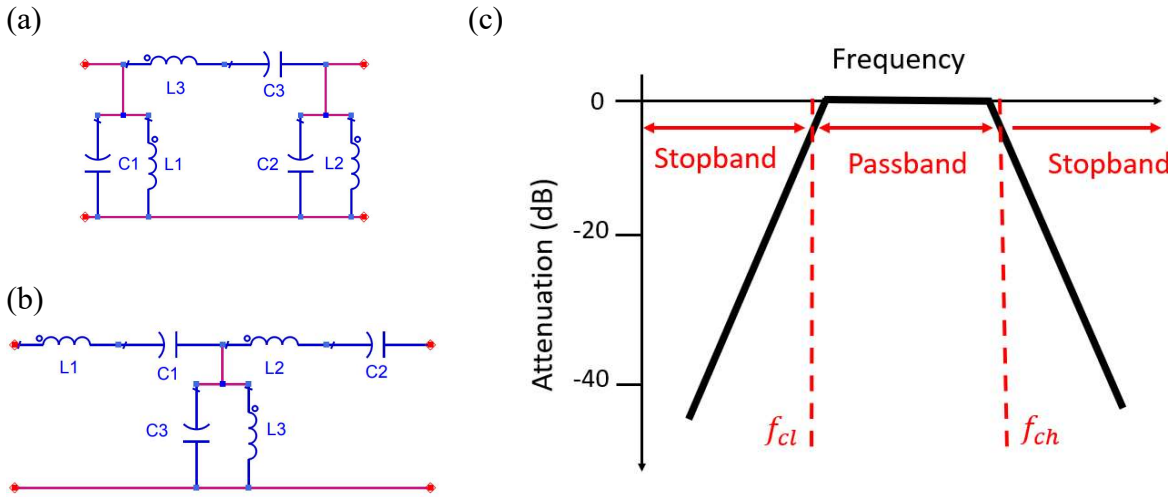

Fig. 1.10. Passband filter. (a) and (b) are pi and T lumped element filters, respectively. (c) General frequency response of passband filters [24].

1.3.4 Bandstop filters

Bandstop filters pass frequency components lower than a desired cutoff frequency and higher than a bigger cutoff frequency. The frequency components between lower and upper cutoff frequencies are rejected. In Fig. 1.11, general structures of bandstop filters are shown in conjunction with the frequency response in which f_{cl} and f_{ch} are the lower and upper cutoff frequencies.

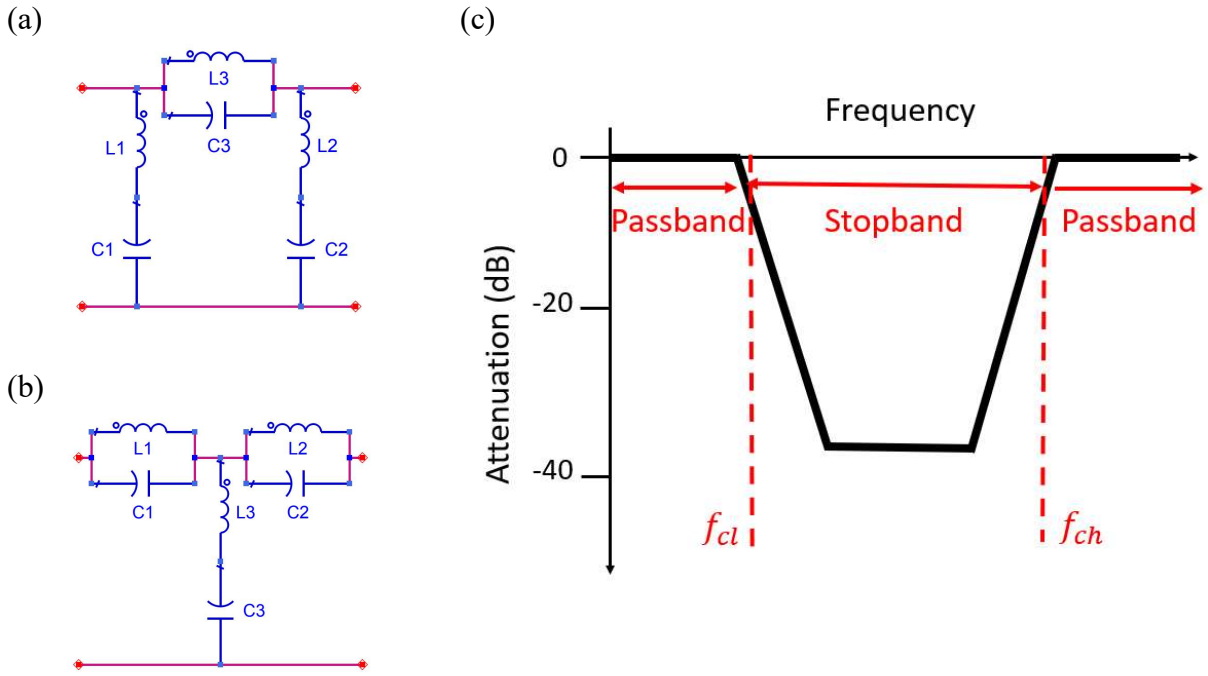

Fig. 1.11. Bandstop filter. (a) Pi model. (b) T model. (c) frequency response [24].

Bandpass and bandstop filters are based on resonant LC tanks. The resonant frequency of LC tanks is $f_r = 1/(2\pi\sqrt{LC})$. At this frequency, the series connection of LC behaves like a short circuit and the parallel connection of LC behaves like an open circuit. These characteristics result in passing and or rejecting middle frequency components.

If there is one series or parallel LC tank, like Fig. 1.12(a) and (b), the frequency response of the bandstop filter becomes sharp at the resonant frequency, f_r, of the LC tank. This kind of filter is known as a notch filter. The frequency response of split-ring resonators (SRRs) is similar to the LC tank notch filter, so SRRs can be used in filter applications. In the next section, split-ring resonators and their applications as filters are explained.

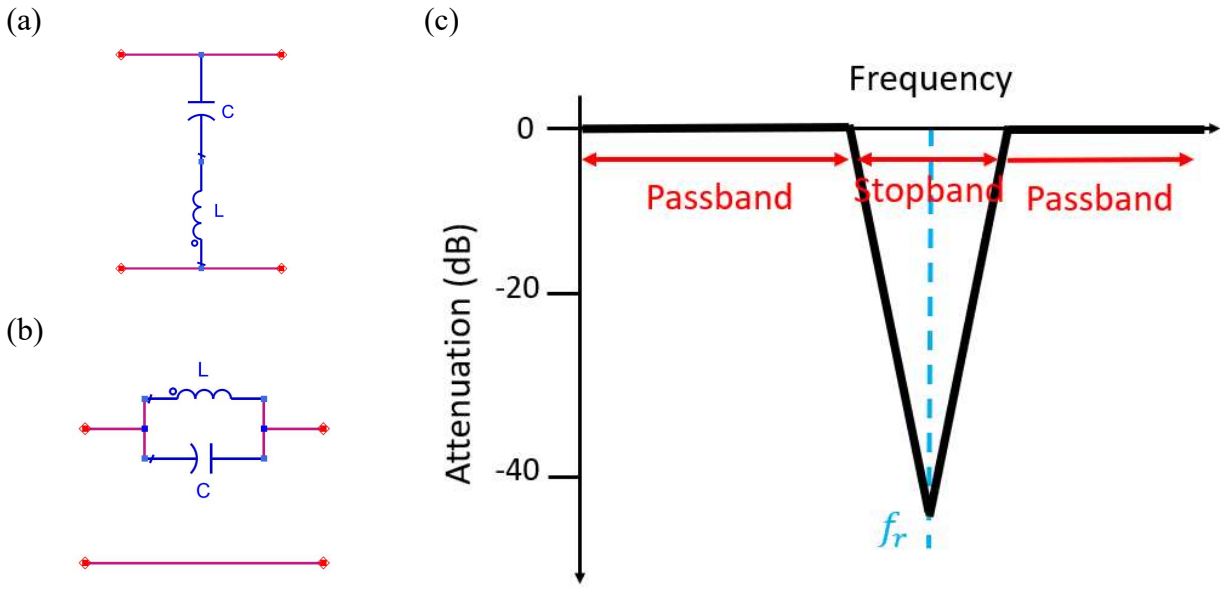

Fig. 1.12. Notch bandstop filter. (a) Series, and (b) parallel circuits. (c) Frequency response.

1.3.5 Phase of the frequency response

In the frequency domain, feeding an input signal $X(j\omega)$ to a filter with a frequency response of $H(j\omega)$, leads to an output $Y(j\omega)$ as follows:

$$Y(j\omega) = H(j\omega)X(j\omega). \tag{1. 3}$$

Which could be explained and analysed based on the amplitude response, $|Y(j\omega)|$, and phase response, $\measuredangle Y(j\omega)$, of the output signal.

$$|Y(j\omega)| = |H(j\omega)||X(j\omega)|, \tag{1. 4}$$

$$\measuredangle Y(j\omega) = \measuredangle H(j\omega) + \measuredangle X(j\omega). \tag{1. 5}$$

As a result, the output of a filter is modified according to the amplitude and phase response of the filter. The phase response $\measuredangle H(j\omega)$ (also known as *phase shift*) can alter the relative phase relationships between the input components, which might lead to substantial changes in the time domain behavior [25].

Over the passband of a filter, the phase response of the filter plays an important role. Assuming that over the passband of a filter $|H(j\omega)| = 1$, meaning that there is no attenuation nor amplification. In this case, if the phase shift is linearly a function of ω, the output of the filter is a copy of the input with a time shift. For example, if $H(j\omega) = e^{-j\omega t_0}$,

$$|H(j\omega)| = 1 \text{ and } \measuredangle H(j\omega) = -\omega t_0, \quad (1.\ 6)$$

$$Y(j\omega) = e^{-j\omega t_0}\, X(j\omega). \quad (1.\ 7)$$

And in the time domain, the output of this filter is

$$y(t) = x(t - t_0), \quad (1.\ 8)$$

which shows that the output of the filter is a replica of the input with a t_0 shift in time.

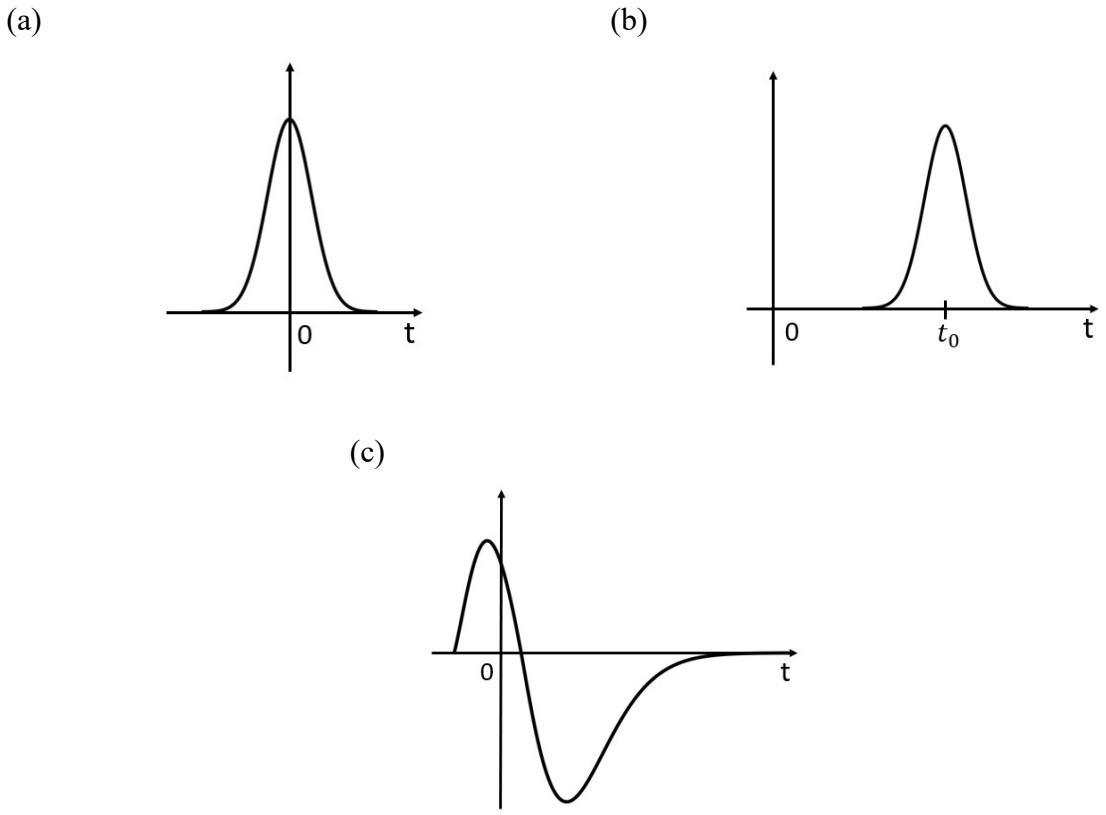

Fig. 1. 13. Response of an all-pass filter to an input signal over the passband. (a) The input signal. (b) The output of the filter if the phase shift of the filter is a linear function with frequency. (c) The output of the filter when the phase shift of the filter is anon-linear function of frequency [25].

This concept is illustrated in Fig. 1. 13 in which Fig. 1. 13(a) is an input to an all-pass filter (all frequency components are passed without any attenuation). If the phase shift of the filter, $\measuredangle H(j\omega)$, is a linear function of ω, the output of the filter is a shifted copy of the input in time, shown in Fig.

1. 13(b). On the other hand, if $\measuredangle H(j\omega)$ is a nonlinear function of ω, the frequency components of the input signal will be shifted with different values so that the frequency components of the output signal are not in their original relative phases, which this leads to the signal distortion as is shown in Fig. 1. 13(c) [25]. An ideal filter would exhibit no insertion loss within the passband, provide infinite attenuation in the stopband, and maintain a linear phase response in the passband to prevent signal distortion [18].

1.4 Split-Ring resonators in metamaterials

When discussing SRRs the concept of metamaterials (MTMs) commonly arises since they are frequently used as an element in an MTM lattice. This thesis focuses on the bandstop filtering aspect of SRRs but given the common link between SRRs and MTMs, this section provides a background on the prior works that use SRRs as 'meta-atoms' in MTMs. MTMs are made of natural materials such as copper or gold in an engineered combination of size and periodicity such that the whole structure behaves differently from each constitutive material. In other words, the new structure is considered as an artificial structure with properties not usual in nature. MTMs were first introduced in 1967 with the speculation on the presence of "substances with simultaneously negative values of ϵ and μ" by Viktor Veselago [26]. Veselago called these "substances" left-handed (LH) to explain that the propagation of electromagnetic waves containing the electric field and magnetic fields, and the phase constant vectors could obey from the left-handed triad, compared to the right-handed triad as electromagnetic waves propagate in the conventional materials. According to resonances created by electromagnetic waves incident to the MTMs, MTMs can show permittivity and permeability with switched values, potentially negative or zero [9]. Therefore, these artificial class of materials can improve the flexibility of controlling of electromagnetic waves and are designed to exhibit specific electromagnetic characteristics at desired frequencies [1].

The first MTM based on split-rings, illustrated in Fig. 1. 14, was made by Pendry et al. [27]. They showed that although the structure is made of conducting metal (non-magnetic), it responds like a magnetic material and shows different magnetic permeability (μ_{eff}) including negative values. They excited this structure with radiated planes waves in a direction that the magnetic field of the EM wave must be perpendicular to the plane of rings so that a current flows in the rings and contributes to a magnetic dipole moment. The magnetic dipole moment oscillates with the frequency of an incident electromagnetic wave, and at a specific frequency it reaches to its maximum value. Which this frequency is called resonant frequency. Structures containing split-rings excited by EM waves are called Split-Ring Resonators (SRR). The response of μ_{eff} of Pendry's structure is depicted in Fig. 1. 15.

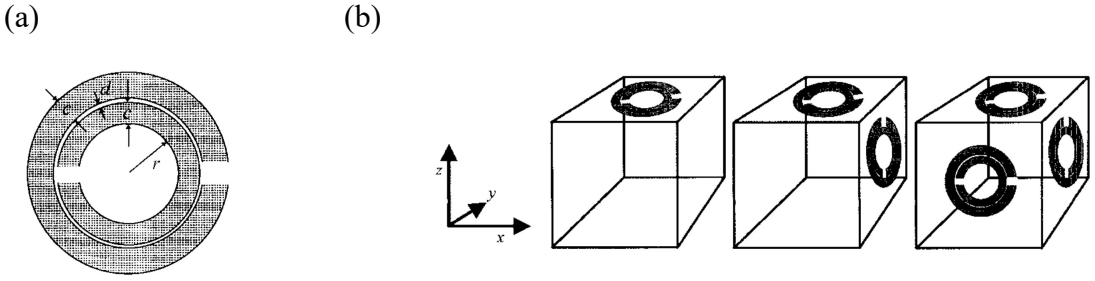

Fig. 1. 14. The first metamaterial in the form of two split-rings. (a) A metamaterial containing two split-rings. (b) Split-rings in one, two, and three dimensions. c, d, and r are width of rings, distance between rings, and the radius of the inner ring, respectively [27] © [1999] IEEE.

Pendry et al. have also introduced negative permittivity (ϵ_{eff}) metamaterials by making a structure containing rods [28], [29], shown in Fig. 1. 16. This type of metamaterials is not covered in this thesis, yet it is worthy of explanation how they work. In rod type metamaterials, the electric field is parallel with rods so that an electric dipole moment is induced in the rods causing a current to flow in the rods. This case shows a plasmonic-type permittivity which is a function of frequency and over a range, permittivity becomes negative [30]. For the first time, Smith et al. created left-handed metamaterial (negative ϵ_{eff} and negative μ_{eff}) by combining SRR and rods [31].

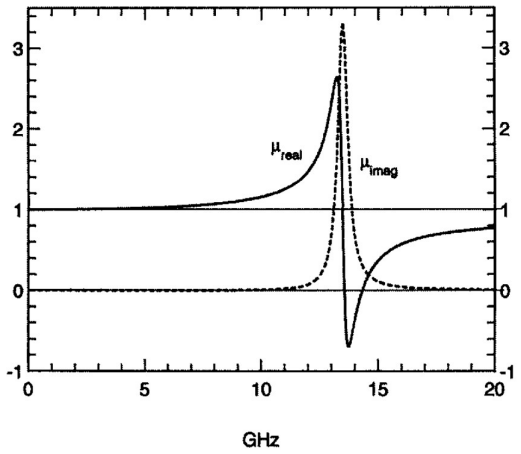

Fig. 1. 15. Plot of μ_{eff} for a split-ring structure depicted in Fig. 1. 14 [27] © [1999] IEEE.

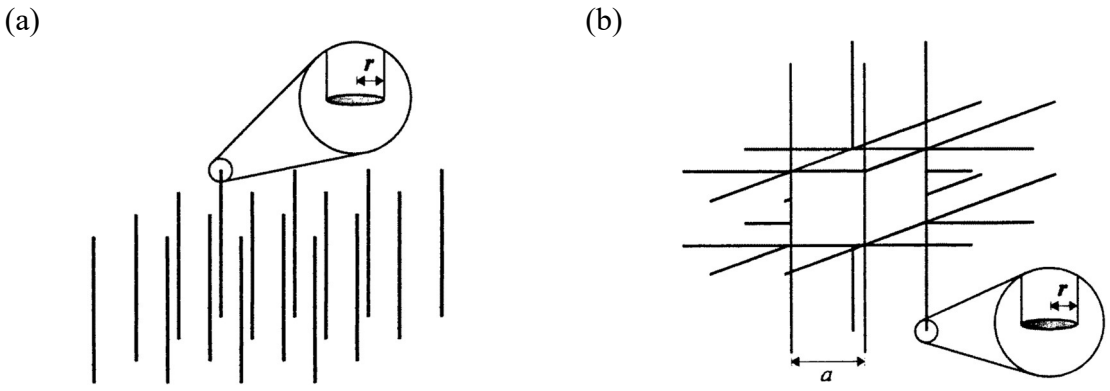

Fig. 1. 16. The first structures made of metallic rods with response of negative (ϵ_{eff}) [28], [29].

Many other works based on SRRs have been presented with different shapes and applications. For example, in Fig. 1. 17, a few metamaterials based on different SRR structures are presented. Fig. 1. 17 (a) shows combination of SRRs with rods to create negative index response [32]. Fig. 1. 17 (b) is a single SRRs [33]. Fig. 1. 17 (c) and (d) are another geometries of SRRs used in a study of electrically resonant MTMs [34].

A metamaterials' electromagnetic response is obtained from the geometries of these resonating elements such as the radii, thickness, and period of the meta-atoms. This differs from materials where the electromagnetic response is given by the atomic or molecular structure [35]. Negative permeabilities are rare in the nature. For instance, negative permeability is obtainable owing to magnetic resonances in ferromagnets at sub-microwave frequencies. However, thin rods and SRRs, below infrared frequencies, can make it possible to acquire desired permittivity and permeability characteristics [1].

Split-ring resonators and other MTMs can be modelled by a resonant RLC circuit (explained in Chapter 2). In their simplest form (identical periodic unit cells), they behave like the notch filter's circuit in Fig. 1.12.

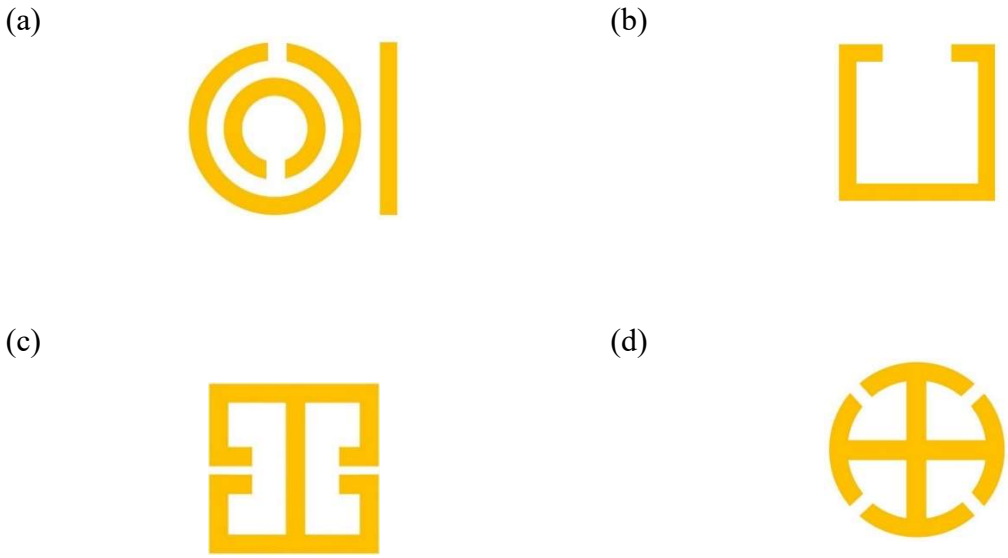

Fig. 1. 17. Four samples of MTM structures. (a) SRRs with rods to create negative index [32]. (b) A single SRR [33]. (c) and (d) SRRs used to study electrical resonance in MTMs [34].

1.5 Split-Ring Resonator Based Transmission Line Filters

The sub-wavelength size of SRRs makes it possible to fabricate them along transmission lines (TLs) so that SRRs' effective parameters modify the whole systems effective parameters, which is equivalent to integrating the SRRs' equivalent circuit to TL's circuit. This means that placing SRRs alongside a TL will result in a frequency dependent transmission response which can be used in filtering applications. In this part of the introduction, filters based on SRRs loaded to TL are studied. It should be noted that the motivation for the following past literature is to verify MTM applications in filtering and less concerned with concepts such as negative permittivities and permeabilities. Also, it is important to recognize that much of this past literature focused on microwave frequencies where instrumentation such as vector network analyzers are readily available for performing device characterization. This work focuses on guided-wave THz structures which adds significant challenges.

In 2003, Martin et al. presented the first coplanar waveguide (CPW) loaded with SRRs and metallic wires, depicted in Fig. 1. 18 [36]. The center strip (with width W) is the signal propagation line which is separated by the gap (G) from top and bottom lines which are ground. Thin wires connect signal strip to ground strips, and SRRs are coincident with wires and fabricated on the back side of the substrate. This structure is a left-handed metamaterial since thin wires contribute to negative ϵ_{eff} and SRRs bring negative μ_{eff}. The frequency response of Fig. 1. 18 is shown in Fig. 1. 19. Considering the frequency response, this structure behaves like a bandpass filter. They also showed that by removing the wires between ground and signal strips, the structure acts like a bandstop filter, Fig. 1. 20.

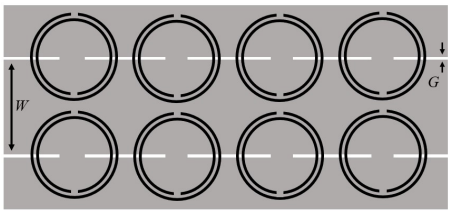

Fig. 1. 18. CPW loaded with SRRs and thin wires [36].

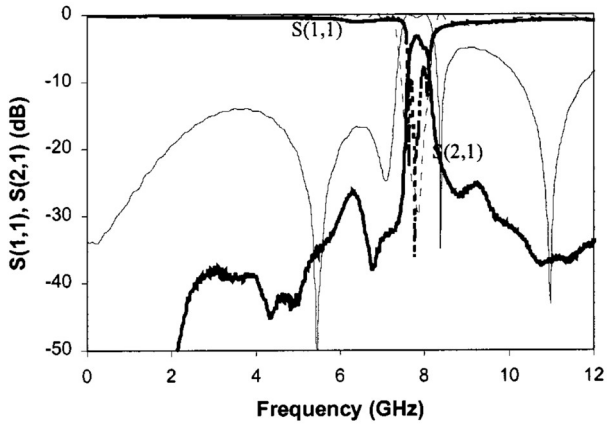

Fig. 1. 19. S11 and S21 parameters of the structure depicted in Fig. 1. 18. Solid lines are measurement, and thin lines are simulation [36].

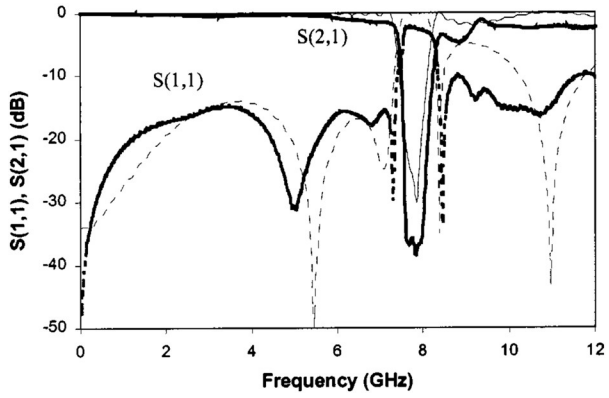

Fig. 1. 20. S11 and S21 parameters of the structure depicted in Fig. 1. 18 without wires between the middle and top and bottom strips. Solid lines are measurement, and thin lines are simulation [36].

A year after, in 2004, they showed that it is possible to etch SRRs on the ground plane and get frequency responses similar to structures in which SRRs are made of conducting medium. These type of etched SRRs are called Complimentary SRRs (CSRR), illustrated in Fig. 1. 21(b) [37], which are easier to fabricate with microstrip transmission lines [38]. In Fig. 1. 22, a CSRR which is etched on the ground plane (black) is couple to a transmission line (gray), and the frequency response of this CSRR is shown in the figure [39].

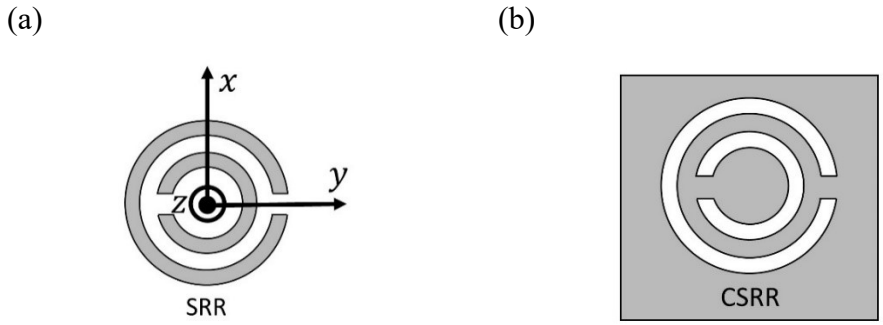

Fig. 1. 21. (a) Split-ring resonator. (b) Complimentary split-ring resonator, etched on the ground plane [37].

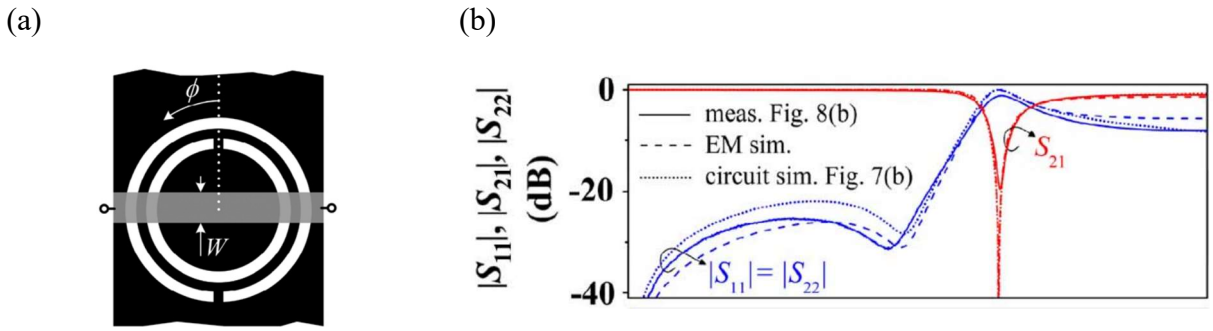

Fig. 1. 22. (a) A CSRR is fabricated on the ground plane (black). (b) S-parameter response which is a bandstop filter [39] © [2013] IEEE.

Loading SRRs to TL in conjunction with TL components like capacitive gaps and stub inductances, Fig. 1. 23(a), was another way to realize filters, introduced by Gil et al. [40].

Frequency responses of the structure in Fig. 1. 23(a) for one, three, and four stages of the cell are depicted in Fig. 1. 23(b).

(a) (b)

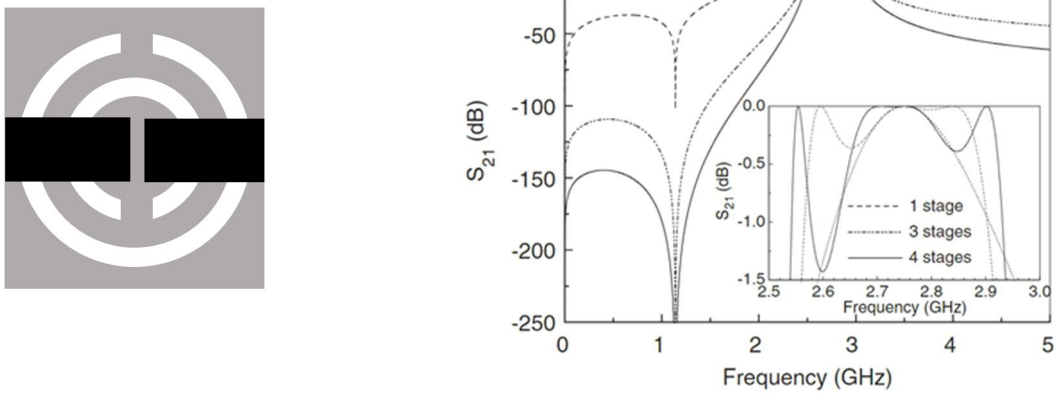

Fig. 1. 23. Frequency response of a microstrip transmission line loaded with CSRR. (a) A unit cell. (b) Frequency responses of one, three, and four stages the unit cell [40].

After successful implementation of filters based on SRRs in conjunction with thin inductive short circuits or capacitive gaps, another strategy was combining these two structures on the same TL. Considering this combination, in Fig. 1. 24, a CPW loaded with SRRs on the substrate is shown. Black color is metallic CPW on top layer, and gray is metallic parts on the substrate. Fig. 1. 24(a) has an inductive short circuit connections between the ground lines of CPW making this unit a left-handed cell, and Fig. 1. 24(b) has a capacitive gap in the center line of CPW [38], [41]. Combining these two cells contributes to Fig. 1. 25(a) composed of one SRR-CPW with a capacitive gap and two SRR-CPW with short circuit stubs. The frequency response of this combination is depicted in Fig. 1. 25(b) which is a bandpass filter.

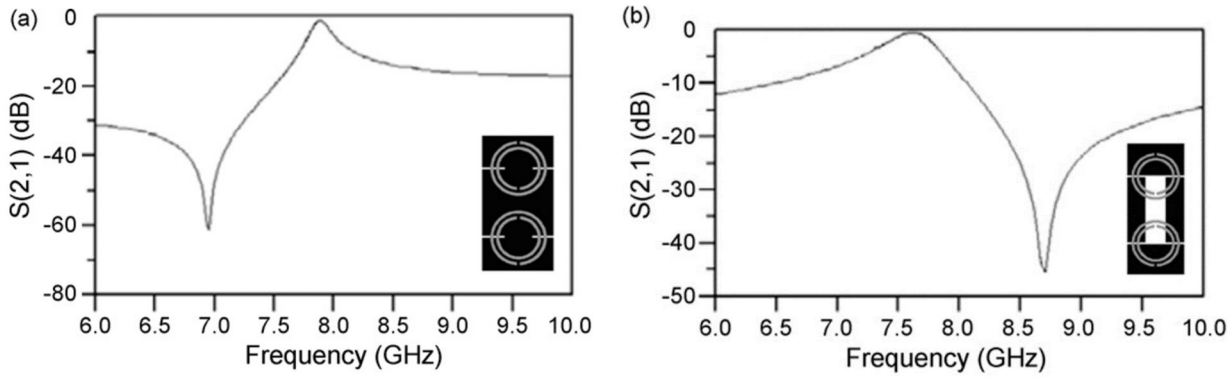

Fig. 1. 24. (a) S21 parameter of a CPW line loaded with SRR and a wire connection between grounds. (b) S21 parameter of a CPW line loaded with SRR and a capacitive gap in signal line [38].

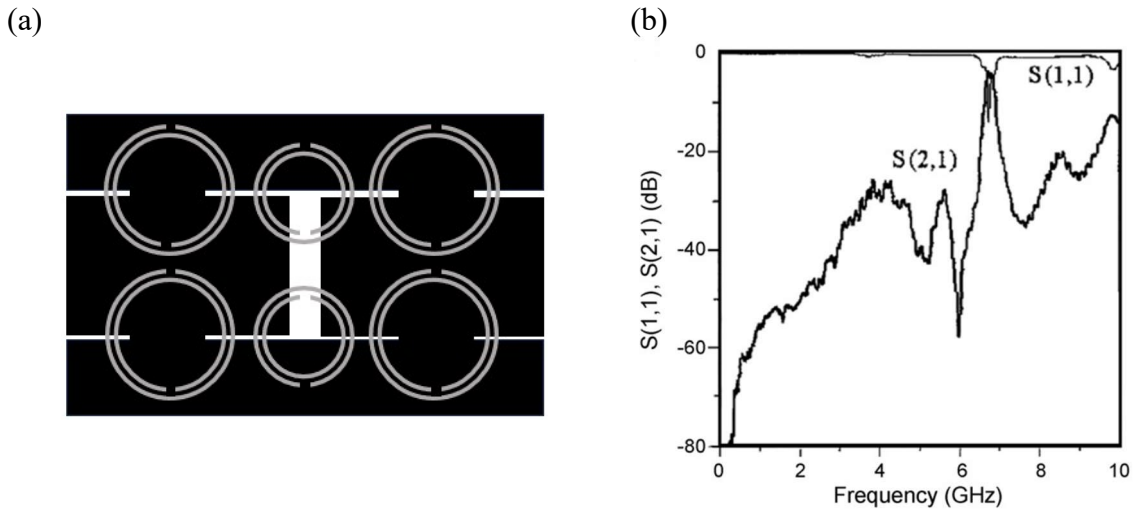

Fig. 1. 25. Layout of the SRR-CPW structure and the frequency response. (a) The center unit contains a capacitive gap, and the side units contain wire shorted lines. (b) The frequency response [38], [41].

Due to advantages of CPS transmission lines, there have been numerous works studying loading SRRs to CPS. The first CPS coupled to SRRs was presented by Ponchak in 2018, Fig. 1. 26 [42]. In this figure, two different orientations are fabricated on the same plane. Fig. 1. 26(b), in which SRRs are rotated by 180 degrees, is named flipped SRR. Ponchak showed that the orientation of SRRs affects the resonant frequency and the level of attenuation. In Fig. 1. 27, S-parameters of this experiment are illustrated. In this figure, black and red lines are corresponding to Fig. 1. 26(a) and Fig. 1. 26(b), respectively. As Fig. 1. 27 illustrates, resonant frequency of the

normal structure and the flipped SRRs differ by almost 1 GHz, and flipped SRRs cause slightly more attenuation.

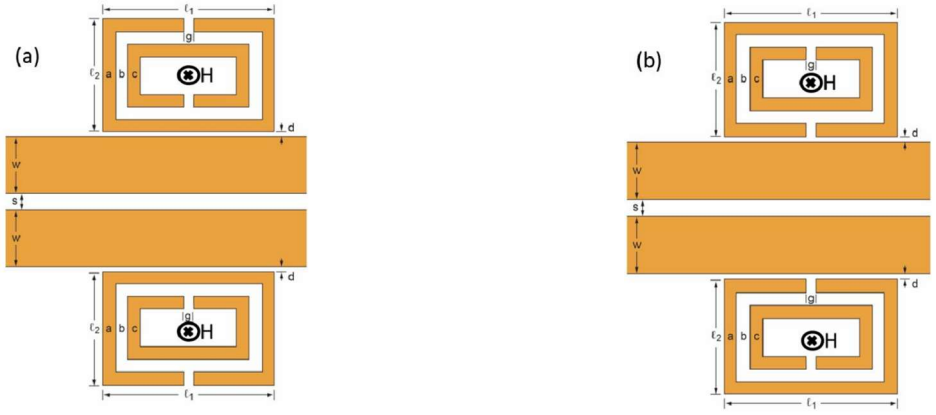

Fig. 1. 26. CPS and SRRs are fabricated on the same plane. (b) SRRs are flipped compared to SRRs in (a) [42] © [2018] IEEE.

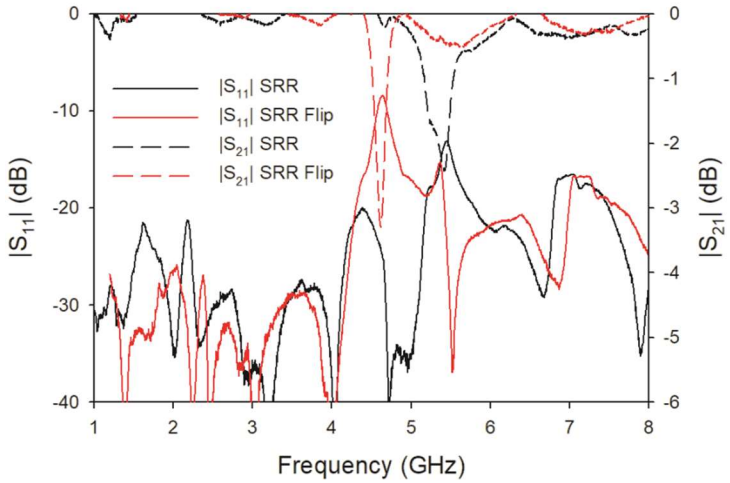

Fig. 1. 27. S-parameters of structures depicted in Fig. 1. 26. Black lines are responses of Fig. 1. 26(a) and red lines are s-parameters of Fig. 1. 26(b) [42] © [2018] IEEE.

In 2021, Smith et al. demonstrated a notch bandstop filter by loading CPS with three SRRs, illustrated in Fig. 1. 28 [43]. The transmission line and SRRs are made of gold, and the substrate is $1\mu m$ Si_3N_4. They conducted this experiment by terahertz time domain spectroscopy. Results of their experiment are shown in Fig. 1. 29, in which Fig. 1. 29(a) is a pico-second pulse received at the receiver, and Fig. 1. 29(b) is the Fourier Transform of the receives pico-second pulse. The latter shows a bandstop notch filter with the first harmonic resonant frequency of 500 GHz.

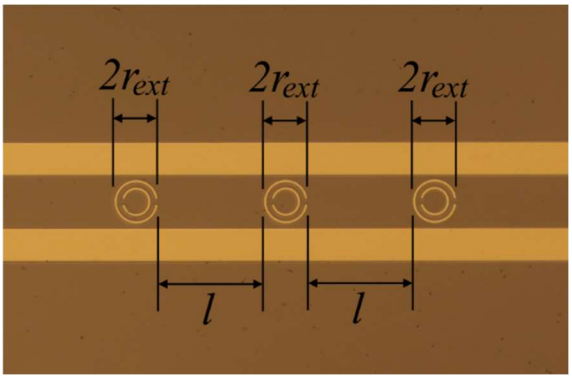

Fig. 1. 28. Three double-SRRs are placed inside a pair of CPS (all on the same plane). [Reprinted] with permission from [43] © Optical Society of America.

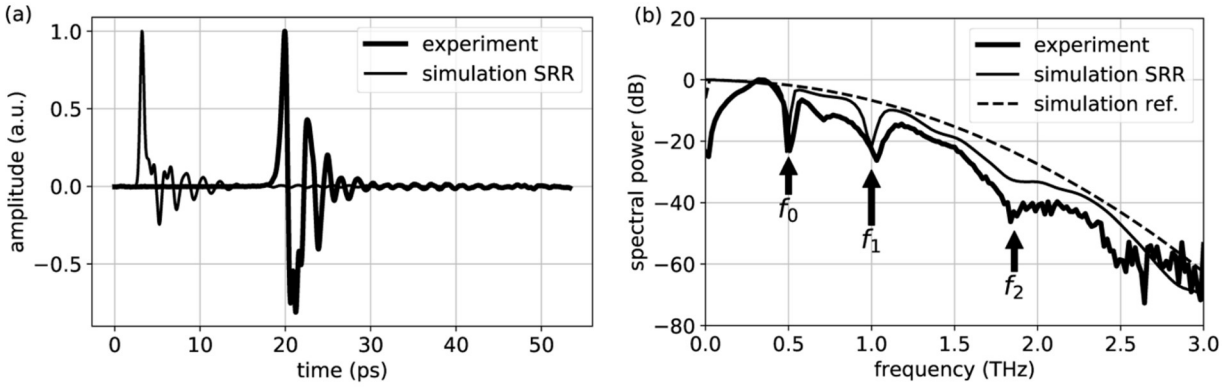

Fig. 1. 29. Time and frequency domain responses of Fig. 1. 28. (a) A pico-second pulse received at the receiver. (b) Fourier Transform of the pico-second pulse. [Reprinted] with permission from [43] © Optical Society of America.

In one of the recent research projects, Shaterian and Mrozowski designed a bandstop notch filter by loading microstrip line with single SRRs, Fig. 1. 30. They also showed that by moving the plane, containing SRRs, the phase of reflection coefficient will change, as a result, a displacement sensor as well as a notch bandstop filter are combined in one design [44]. In Fig. 1. 31, the frequency response and the phase of the reflection coefficient are shown. The resonant frequency and bandwidth are about 4.9 GHz and 0.36 GHz, respectively.

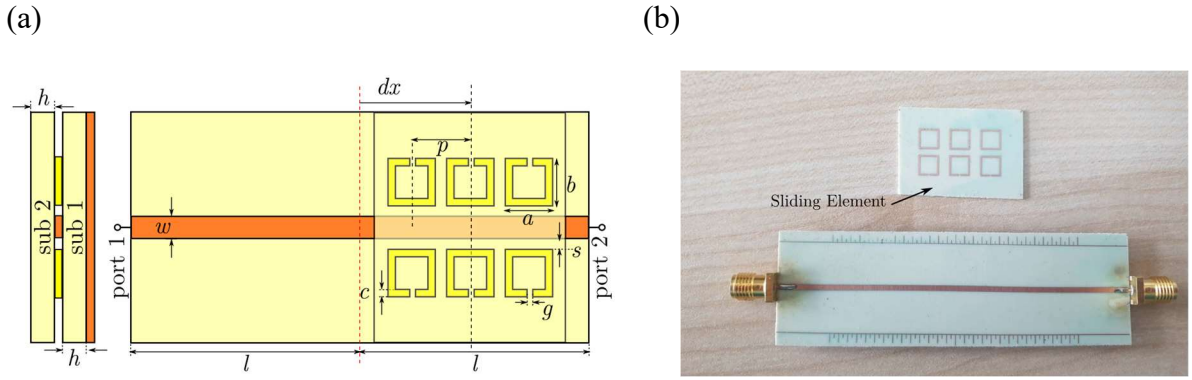

Fig. 1. 30. (a) Side and top views of the filter/sensor structure. (b) The fabricated structure [44] © [2023] IEEE.

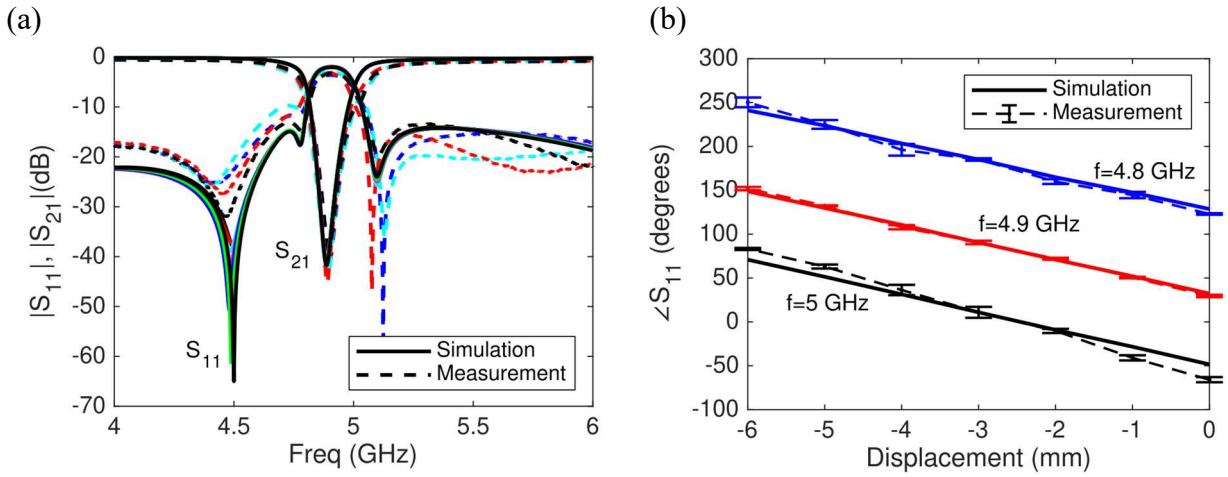

Fig. 1. 31. (a) S21 and S11 responses of the structure presented in Fig. 1. 30. (b) Phase of the reflection coefficient with displacement of SRRs in Fig. 1. 30 [44] © [2023] IEEE.

As it is seen in the presented examples, many works including transmission lines loaded with SRRs have been conducted. The research in this thesis is conducted by getting inspired from the research shown in Fig. 1. 28, and the aim was widening the rejection band so that the filter could behave like a wide-bandstop filter. The results of the research in this thesis are presented in the Results and Discussion chapter.

Chapter 2

Theory of SRR and Modeling

This chapter examines the theory and modelling of SRRs, and transmission lines loaded with SRRs.

2.1 Theory of SRR

The purpose of this section is to provide the background associated with SRRs that is typically obtained in the context of MTMs. Hence, this thesis provides the analysis that is found when discussing SRRs to construct a negative permeability MTM as it contains useful modelling concepts.

Considering a *closed* metallic ring on which an external time varying magnetic field is applied perpendicular to the ring's plane, the external magnetic field induces an alternating current in the ring, which generates an induced magnetic flux which opposes the changes in the external magnetic field (Lenz's law). Which means, the magnetic polarizability of the ring is negative creating a negative dipole moment and magnetic susceptibility (diamagnetism). The induced magnetic dipole moment, m_z, and magnetic polarizability, α_{zz}^{mm}, of a lossless conducting ring, which are along its axis, are [45]

$$m_z = \alpha_{zz}^{mm} B_z^{ext} \qquad (\text{A.m}^2), \tag{2. 1}$$

$$\alpha_{zz}^{mm} = -\frac{\pi^2 r^4}{L} \qquad (\text{m}^4/\text{H}). \tag{2. 2}$$

The sub-index zz means the external force is along the z-axis, and the produced effect is along the z-axis as well. And the super index mm means the external force is magnetic, and the result is magnetic. B_z^{ext} is the external magnetic field, along the z-axis, applied to the closed ring. r and L are the radius and inductance of the ring, respectively. The inductance of a perfect conductor ring is [45]

$$L = \mu_0 r \left[\ln\left(\frac{16r}{d}\right) - 2\right] \qquad \text{(H)}. \tag{2. 3}$$

where d is the width of the ring. Since normally r is bigger than twice of d then $L \geq \mu_0 r$. Hence, $-\pi^2 r^3 \leq \mu_0 \alpha_{zz}^{mm} < 0$. The magnetic susceptibility χ_m (approximated by $\chi_m \approx \frac{\mu_0 \alpha_{zz}^{mm}}{Vol}$, which $Vol \geq (2r)^3$ is the volume of the ring) becomes $-1 \approx -\frac{\pi^2}{8} \leq \chi_m < 0$. Then by explaining effective permeability as:

$$\mu_{\text{eff}} = \mu_0(1 + \chi_m) \qquad \text{(H/m)}. \tag{2. 4)9}$$

It is seen that closed metallic rings do not create a considerable negative μ_{eff}. In other words, the diamagnetic effect of closed metallic rings is not powerful enough to generate negative μ_{eff} [45].

Nevertheless, loading capacitance element into the ring could result in an increase in the magnetic polarizability [46] which is discussed next. The structure of a ring containing a capacitive gap is called split-ring resonator (SRR), shown in Fig. 1. 14 [27]. There is expected a strong diamagnetic behavior above the resonant frequency of the SRR with external magnetic field perpendicular to the plane of the SRR. As a result, SRRs show negative permeability over specific frequency range [41]. For convenience, Fig. 1. 14 with considering the charge accumulation on SRRs is illustrated here as Fig. 2. 1. In this figure, rings are coupled to each other capacitively through their edges, and the external magnetic and electric fields are in the z-axis and y-axis directions, respectively.

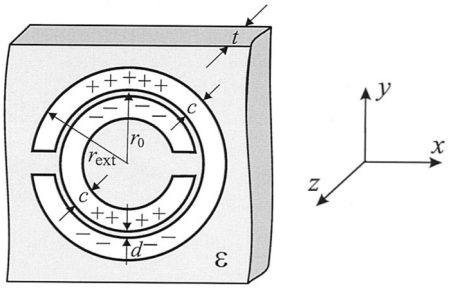

Fig. 2. 1. A coupled pair of SRR [47] © [2003] IEEE.

Because of the external magnetic field, current flows on each ring, and due to the split on each ring, the currents must flow from one ring to the other through the split gaps such that it can

be said an alternating current is flowing over the two rings. The whole structure contains capacitance, due to the slot between the rings, and inductance. The capacitance of the splits (or cuts) is negligible compared the capacitance between the split-rings. Hence, the behavior of the SRR can be approximated by a combination of capacitor and inductor like LC circuits. This circuit is valid if the length of the SRR is much smaller than the applied wavelength. Based on these assumptions, the current on each ring comes to zero at the split location, and the change of current on each ring, by moving from split to the other side, can be considered linear so that the total current on the SRR (consisting of two split-rings) is constant [45].

The total capacitance between the rings is distributed, and there are stronger electric fields at the top and bottom of SRR between rings. Hence, the total capacitance between two rings can be considered as two capacitances of the same value for upper and lower half rings. By considering the total inductance of the split-rings, the circuit shown in Fig. 2. 2 is the equivalent circuit model of the SRR in which it is assumed losses are negligible [45] and [48]. L_s is the total inductance of the SRR, $C_0 = 2\pi r_0 C_{pul}$ is the total capacitance between rings, C_{pul} is capacitance per unit length between rings, and r_0 is the average radius of the SRR structure. In this regard, $C_0/2$ is the capacitance between upper and lower half rings, and Φ_m is an external magnetic flux passing through the SRR [48]. The equation for the total current on the SRR, or equivalently in the circuit, is expressed in (2. 5) in which Σ is the external excitation [45].

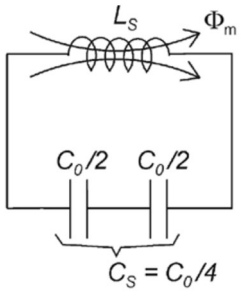

Fig. 2. 2. The equivalent circuit of a SRR [48] © [2005] IEEE.

$$\left(\frac{1}{j\omega\, C_0/4} + j\omega L_s\right) I \approx \Sigma \qquad \text{(V)}. \tag{2. 5}$$

By solving (2. 5) for $\Sigma = 0$, the resonant frequency of the SRR, ω_0, can be obtained from (2. 6). The magnetic external excitation formula of SRR is expressed in (2. 7). By combining (2. 5) to (2. 7), and for simplicity using equality sign (=) instead of approximately sign (≈), an equation for the total current on the SRR is obtained in (2. 8).

$$\omega_0^2 \approx \frac{4}{C_0 L_s} = \frac{2}{\pi r_0 L_s C_{pul}} \quad \text{(rad/s)}^2, \tag{2. 6}$$

$$\Sigma = -j\omega\Phi_m \quad \text{(V)}, \tag{2. 7}$$

$$I = \frac{\Phi_m}{L_s}\left(\frac{\omega_0^2}{\omega^2} - 1\right)^{-1} \quad \text{(A)}. \tag{2. 8}$$

The magnetic dipole moment, m_z, and the external magnetic flux passing over the SRR, Φ_m, are as follows in which B_z^{ext} is the external magnetic field.

$$m_z = \pi r_0^2 I \quad \text{(A.m}^2\text{)}, \tag{2. 9}$$

$$\Phi_m = \pi r_0^2 B_z^{ext} \quad \text{(Wb)}. \tag{2. 10}$$

Using (2. 1) and (2. 8) to (2. 10), polarizability and magnetic dipole moment for split ring resonator are obtained in (2. 11) and (2. 12).

$$\alpha_{zz}^{mm} = \frac{\pi^2 r_0^4}{L_s}\left(\frac{\omega_0^2}{\omega^2} - 1\right)^{-1} \quad \text{(m}^4\text{/H)}, \tag{2. 11}$$

$$m_z = \frac{\pi^2 r_0^4}{L_s}\left(\frac{\omega_0^2}{\omega^2} - 1\right)^{-1} B_z^{ext} \quad \text{(A.m}^2\text{)}. \tag{2. 12}$$

(2. 11) and (2. 12) clarify that by approaching the resonant frequency of a SRR, ω_0, there is a large variation in the polarizability and magnetic dipole moment of rings with splits (SRR), which the large value cannot be obtained for closed loop rings (equation (2. 1)).

The next step is to include losses into the SRR behavior. Losses associated with rings are mainly ohmic which can be taken into account as the imaginary part of the total inductance as follows [47]

$$\hat{L}_s = L_s + \frac{R}{j\omega} \quad \text{(H)}. \tag{2. 13}$$

In this regard, the resonant frequency of the SRR, expressed in (2. 6), should include $\hat{L}_s$, that means

$$\widehat{\omega}_0^2 \approx \frac{4}{C_0\hat{L}_s} = \frac{2}{\pi r_0 \hat{L}_s C_{pul}}. \tag{2. 14}$$

Where, $\widehat{\omega}_0$ is the resonant frequency of the SRR considering ohmic losses. Next, the following calculations help to find a substitution for $(\widehat{\omega}_0^2/\omega^2 - 1)^{-1}$.

$$\widehat{\omega}_0^2 = \frac{4}{C_0\hat{L}_s} = \frac{4}{C_0\left(L_s + \frac{R}{j\omega}\right)} = \frac{4}{C_0 L_s\left(1 + \frac{R}{jL_s\omega}\right)} = \frac{\omega_0^2}{1 + \frac{R}{jL_s\omega}} = \frac{\omega_0^2}{1 + \frac{\Gamma}{j\omega}} \tag{2. 15}$$

Where $\Gamma = R/L_s$. Then by using the result of (2. 15),

$$\left(\frac{\widehat{\omega}_0^2}{\omega^2} - 1\right)^{-1} = \frac{\omega^2}{\frac{\omega_0^2}{1 - j\frac{\Gamma}{\omega}} - \omega^2} = \frac{\omega^2\left(1 - j\frac{\Gamma}{\omega}\right)}{\omega_0^2 - \omega^2 + j\Gamma\omega} = \frac{\omega_0^2}{\widehat{\omega}_0^2} \times \frac{\omega^2}{\omega_0^2 - \omega^2 + j\Gamma\omega} \tag{2. 16}$$

Next, comparing (2. 6) and (2. 14), it is obtained that $\widehat{\omega}_0^2\hat{L}_s = \omega_0^2 L_s$, so the magnetic polarizability, (2. 11), for lossy SRRs, $\hat{\alpha}_{zz}^{mm}$, becomes

$$\hat{\alpha}_{zz}^{mm} = \frac{\pi^2 r_0^4}{\hat{L}_s}\left(\frac{\widehat{\omega}_0^2}{\omega^2} - 1\right)^{-1} = \frac{\pi^2 r_0^4}{L_s}\left(\frac{\omega^2}{\omega_0^2 - \omega^2 + j\Gamma\omega}\right) \tag{2. 17}$$

Back to equation (2. 4)9, and the first order approximation of magnetic susceptibility ($\chi_m \approx \frac{\mu_0 \hat{\alpha}_{zz}^{mm}}{Vol}$, which $Vol \geq (2r_{ext})^3$ is the volume of the SRR), the effective permeability of rings with split (SRRs) is

$$\mu_{\text{eff}} = \mu_0(1 + \chi_m) = \mu_0\left[1 + \frac{\mu_0\pi^2 r_0^4}{L_s(2r_{ext})^3}\left(\frac{\omega^2}{\omega_0^2 - \omega^2 + j\Gamma\omega}\right)\right]. \tag{2. 18}$$

And by considering F as

$$F = \frac{\mu_0\pi^2 r_0^4}{L_s(2r_{ext})^3} \tag{2. 19}$$

which is less than 1, the effective permeability of the SRR can be written in the following more compact format:

$$\mu_{\text{eff}} = \mu_0 \left[1 + \left(\frac{F\omega^2}{\omega_0^2 - \omega^2 + j\Gamma\omega}\right)\right]. \tag{2. 20}$$

By considering losses negligible, the magnetic permeability has positive and negative values in different frequencies as follows

$$\text{if } \Gamma \approx 0 \rightarrow \ \mu_{\text{eff}} \begin{cases} \leq 0 & \text{for } \omega_0 < \omega \leq \dfrac{\omega_0}{\sqrt{1-F}} \\ > 0 & \text{otherwise} \end{cases} \tag{2. 21}$$

which means in the mentioned narrow band, magnetic permeability is negative. Equation (2. 20) is plotted in Fig. 2. 3 for a single-SRR with a radius of 14 μm, conductance of 55.1 pH, resistance of 5.85 ohms, and meant to resonate at 1 THz. This single-SRR is simulated in the results and discussion section. By approaching ω_0, polarizability becomes very large negative value (2. 11). The latter leads to a large negative magnetic moment (2. 1) [10].

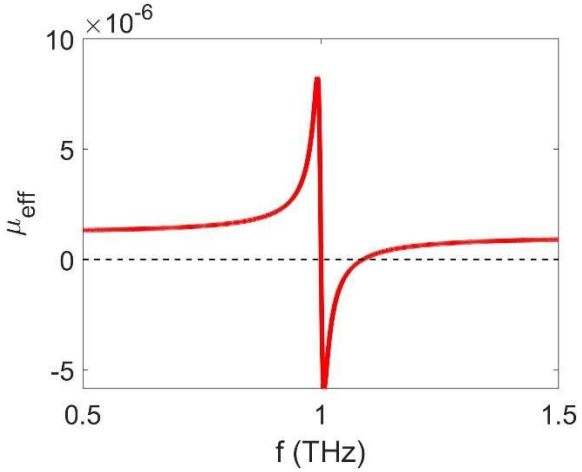

Fig. 2. 3. Effective permeability of a single-SRR. $r = 14\ \mu\text{m}, L = 55.1\ p\text{H}, R = 5.85\ \Omega$, and $f_0 =$ 1 THz. For the frequency portion under the dashed line, μ_{eff} is negative.

Considering Fig. 2. 1. A coupled pair of SRR [47] © [2003] IEEE., a more detailed analysis clarifies that in addition to the magnetic dipole, SRR acts as an electric dipole as well. Applying

an external electric field, leads to accumulation of opposite charges on the upper and lower halves of the SRR as it is shown in this figure, so that SRR has an electric moment in the y-axis. This electric moment causes a current flow on the rings resulting in an additional magnetic moment. In other words, the resonance in the SRR can be created by an external electric field along the y direction as well. This behavior is called cross polarization [49]. The magnetic and electric dipoles resulted from external magnetic and electric fields are

$$m_z = \alpha_{zz}^{mm} B_z^{ext} + j\alpha_{zy}^{me} E_y^{ext} \quad \text{(A.m}^2\text{)}, \tag{2. 22}$$

$$p_y = \alpha_{yy}^{ee} E_z^{ext} + j\alpha_{yz}^{em} B_z^{ext} \quad \text{(C.m)}, \tag{2. 23}$$

$$p_x = \alpha_{xx}^{ee} E_x^{ext} \quad \text{(C.m)}. \tag{2. 24}$$

Where m_z, p_y, and p_x are magnetic dipole in the z direction, electric dipole in the y direction, and electric dipole in the x direction, respectively. α_{zy}^{me} means magnetic polarizability in the z direction due to an external electric field in the y direction, and α_{yz}^{em} means electric polarizability in the y direction due to a magnetic field in the z direction. Similar concept of definition is applied to α_{zz}^{mm}, α_{yy}^{ee}, and α_{xx}^{ee}.

The approximate susceptibilities in x, y, and z directions are $\chi_{exx} \approx \alpha_{xx}^{ee}/Vol$, $\chi_{eyy} \approx \alpha_{yy}^{ee}/Vol$, and $\chi_{mzz} \approx \mu_0 \alpha_{zz}^{mm}/Vol$ [49]. Regarding these approximations and equation (2. 4), in calculation of μ_{eff} in the z direction, α_{zz}^{mm} is required, and also magnetic polarizability is the dominant effect in SRRs behavior which leads to a powerful diamagnetic response [47]. Therefore, neglecting cross polarization effect (α_{zy}^{me}) in analyzing SRRs behavior does not make a big difference. Indeed, electric dipoles play the main role in the complementary split-ring resonators discussed in the previous chapter [39]. The details of cross polarization and extraction of the parameters in (2. 22) to (2. 24) are provided in [47], [49].

2.2 Modeling of SRR and CSRR loaded to transmission lines

Modeling is a technique to explain the behaviour of phenomena based on elements in a simpler form. For example, mass-spring-damper in mechanics and R-L-C circuits in electronics are used in systems with oscillation. Modeling provides us understanding the phenomena from a different point of view which usually is simpler to realize.

2.2.1 Modeling of SRR

As we know from the theory of SRR sub-section that the behaviour SRRs, Fig. 2. 1. A coupled pair of SRR [47] © [2003] IEEE. oscillating at a specific frequency, is similar to resonant LC tanks in electrical circuits. The equivalent circuit of the SRR was illustrated in Fig. 2. 2. Hence, it is possible to analyse SRR behaviour in terms of its equivalent circuit. The total capacitance of a SRR containing two split-rings is $C_0 = 2\pi r_0 C_{pul}$, where r_0 is the average radius of the rings [48]. And the approximated inductance and resonant frequency of SRRs are explained by formulas (2. 3) and (2. 6), respectively. Considering values in these formulas and the equivalent circuit model, the resonant frequency can be written as $\omega_0 = 1/\sqrt{L_s C_s}$, where $C_s = C_0/4$.

2.2.2 Modeling of CSRR

Till here, the model of SRR is obtained. Studying CSRR is not in the scope of this thesis; nevertheless, since CSRRs are the reverse of SRRs, it is worthy to show CSRRs' equivalent model in order to a comparison with SRRs. A CSRR is depicted in Fig. 2. 4 in which the gray plane is the ground plane, and the white is an etched SRR on the ground plane. CSRR is excited by axial electric field and behaves as an electric dipole. If the effect of metal losses and dielectric thickness are neglected, a dual characteristics is obtained for CSRRs with respect to SRRs [37].

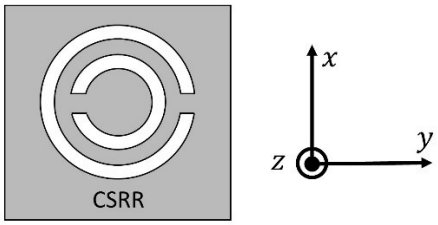

Fig. 2. 4. Complimentary split ring resonator (CSRR) [37].

The circuit model for CSRR is shown in Fig. 2. 5. This model is dual circuit model of the SRR's circuit model. In CSRR model, C_c, which is the capacitance of the disk, is the dual of L_s in SRR. The series connection of two capacitors in the SRR model, is replaced by a parallel connection of two inductors, in CSRR model, connecting inner disk of CSRR to the ground; as a result, C_s is substitute by L_c. In addition, $L_0 = 2\pi r_o L_{pul}$, which L_{pul} is per unit length inductance between ground and the inner disk of CSRR, r_0 is the average radius of the etched rings, and Φ_e is an electric flux from TL ending in CSRR. For ideal dual condition mentioned above, perfect

extremely thin conductors and absence of dielectric, the circuit model of SRR and CSRR are related by $C_c = 4(\epsilon_0/\mu_0)L_s$ and $C_0 = 4(\epsilon_0/\mu_0)L_0$ [48].

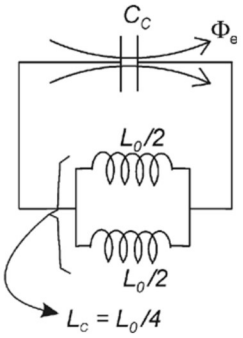

Fig. 2. 5. Equivalent circuit model for a CSRR [48] © [2005] IEEE.

2.2.3 Modeling of TLs loaded with SRR and CSRR

The next step is finding the equivalent circuit of SRRs and CSRRs loaded to a TL. In this regard, first, the equivalent circuit model of TL is shown. The equivalent circuit model for TEM transmission lines of length Δz is depicted in Fig. 2. 6 in which $C', L', R',$ and $G'$are per unit length line capacitance, inductance, resistance, and conductance, respectively. R' is associated to conductor loss, and G'accounts for dielectric loss [24]. The CPS depicted in Fig. 1.3(b) is a TEM TL, so this model can be used for CPS.

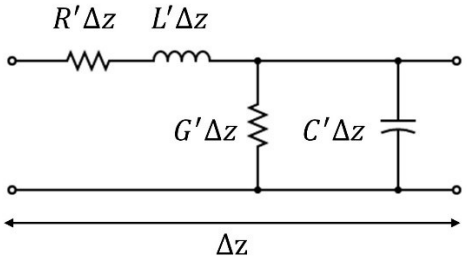

Fig. 2. 6. Equivalent lumped circuit model of a distributed TEM transmission line of length Δz[15], [30].

After knowing models of TL and SRR and CSRR, the next step is explaining a model containing the host TL and loaded SRR or CSRR. Fig. 2. 7 illustrates a section of a coplanar

waveguide (CPW) loaded with two SRRs and the equivalent circuit. This section is called a unit cell. CPW, Fig. 1.3(c), is composed of a signal plane in the middle and two ground planes at the top and down of the structure. In this figure, L and C are the total capacitance and inductance of CPW and L_s and C_s are inductance and capacitance of one SRR. M is the mutual inductance between CPW and a SRR arising from magnetic coupling between CPW and SRR. Due to the symmetry of CPW structure (from P_1 to P_2), the magnetic wall concept could be applied, so half of the unit cell is modeled as shown in Fig. 2. 7(b). The capacitance and inductance of the half of the CPW are $C/2$ and $2L$, respectively [48], [50]. Fig. 2. 7(c) is the equivalent circuit model for Fig. 2. 7(b). The equivalent parameters are depicted from (2. 25) to (2. 28) in which ω_0^2 is the resonant frequency, and f is the fraction of the slot occupied by the SRR.

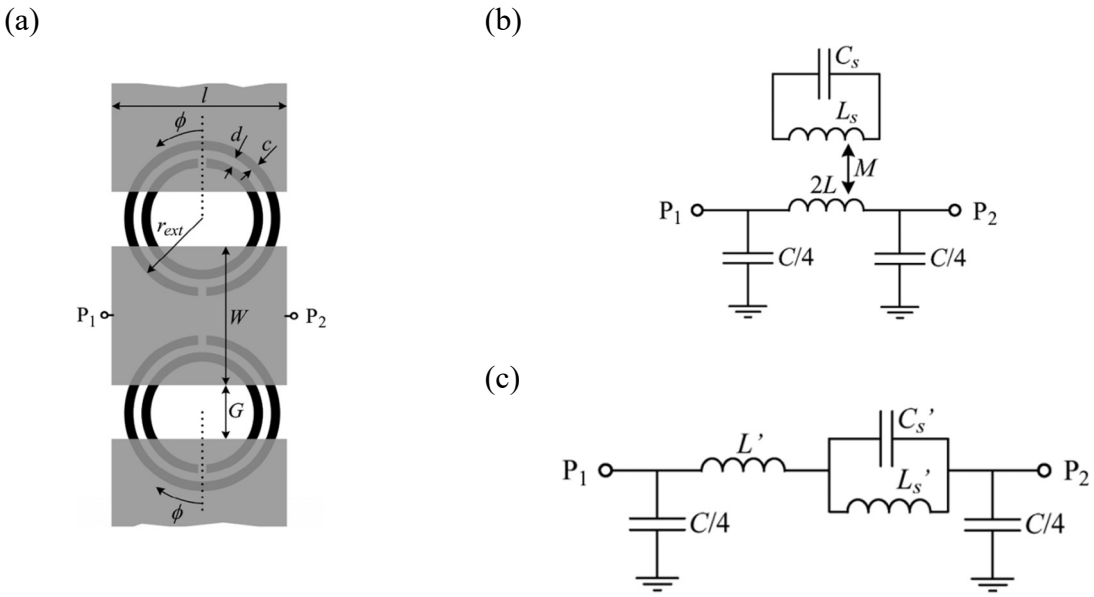

Fig. 2. 7. CPW loaded with two SRRs. (a) One unit cell. (b) Equivalent lumped element circuit model of the unit cell. (c) Equivalent circuit for (b) [39] © [2013] IEEE.

$$C_s' = \frac{L_s}{M^2\omega_0^2} \quad \text{(F)}, \tag{2. 25}$$

$$L_s' = C_s\, M^2\omega_0^2 \quad \text{(H)}, \tag{2. 26}$$

$$\omega_0^2 = \frac{1}{\sqrt{L_s C_s}} \quad \text{(rad/s)}^2, \tag{2. 27}$$

$$M = 2L \times f \quad \text{(H)}. \tag{2. 28}$$

A unit cell of CSRR and its equivalent circuit are depicted in Fig. 2. 8. In this figure, black is the ground plane, white is CSRR (which is etched on the ground plane), and gray is the microstrip TL. CSRR is mainly excited by electric field, so the coupling between TL and CSRR is capacitive. Since CSRR is etched on the ground plane, the circuit model of the structure can be a series connection of the line's capacitance and the $L_c C_c$ resonator tank for the CSRR [48].

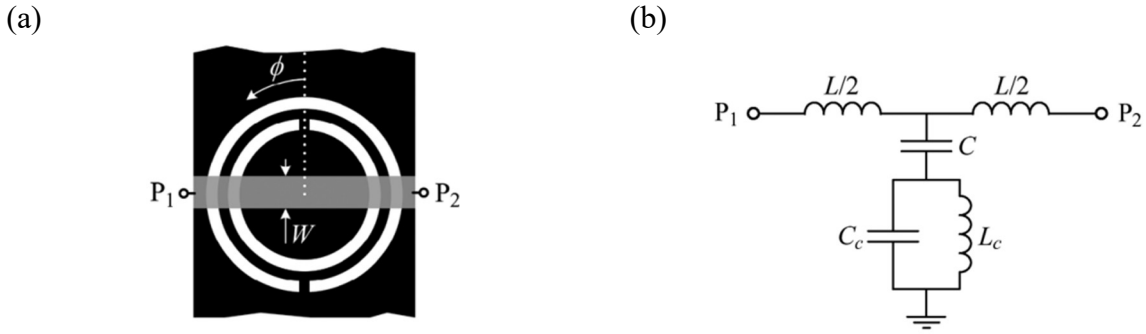

Fig. 2. 8. A microstrip transmission line loaded with a CSRR. (a) A unit cell of CSRR etched on the ground plane. Black is the ground plane, white is CSRR, and gray is a microstrip TL. (b) Equivalent circuit model for (a) [39], [48] © [2005, 2013] IEEE.

The lumped element circuit models for TL loaded with SRR or CSRR presented above are of the first order coupling approximations. For the CPW loaded with SRR, it was considered that the coupling is magnetic and for the microstrip line loaded with CSRR, it was assumed there is an electric coupling between TL and CSRR. However, for both SRR and CSRR, there are electric and magnetic couplings of course with different strength which was talked at the end of the theory of SRR sub-section as the cross polarization. Hence, to have a more exact lumped element circuit model, in addition to the magnetic coupling for SRR, an electric coupling in structures containing SRR should be considered as well. Likewise, by exerting a magnetic coupling to CSRR structures in addition to the electric coupling, a more exact circuit model will be obtained. Fig. 2. 9(a) is a better approximation circuit model for a unit cell of CPW loaded with SRR, depicted in Fig. 2. 7(a). This model contains all the circuit components in the previous model, Fig. 2. 7(b), plus a coupling capacitance C_a, regarding an electric coupling between SRR and TL. The value of C_a is calculated by curve fitting between the circuit simulation and an electromagnetic full wave response. For CSRR a better circuit model approximation is presented in Fig. 2. 9(b). This model is similar to the model in Fig. 2. 8(b), but in order to consider the magnetic coupling, the inductance

of the resonance tank is coupled to the TL. M is obtained by curve fitting of the circuit simulation and an electromagnetic full wave response. All in all, there are both electric and magnetic couplings in TLs loaded with SRR/CSRR. However, for SRR-loaded TLs, the magnetic coupling is dominant, and for CSRR loaded TLs, the electric coupling is dominant [39].

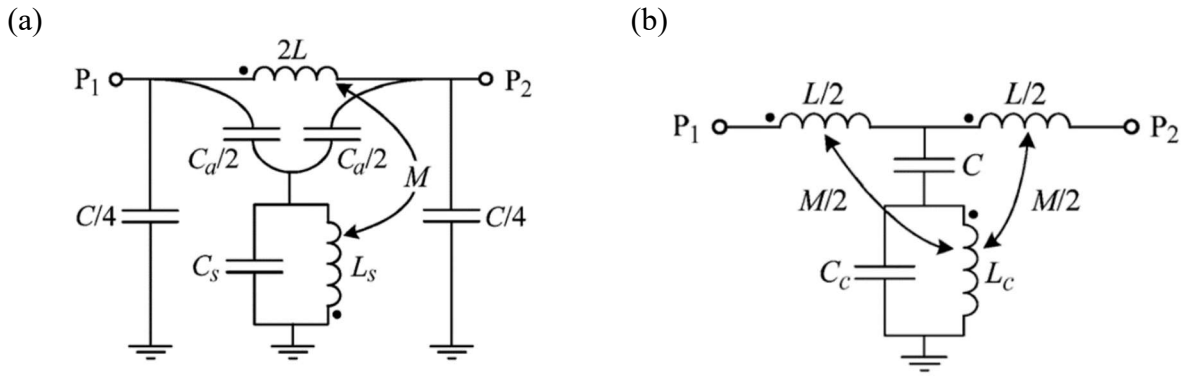

Fig. 2. 9. An improved equivalent circuit model for (a) CPW loaded with SRR, and (b) microstrip TL loaded with CSRR [39] © [2013] IEEE.

Chapter 3

Results and Discussion

This thesis focuses on the design and experimental characterization of a bandstop filter, with the center frequency of 1 THz, that consists of a CPS loaded with nine single SRRs. This chapter is dedicated to discussing the simulations (in ANSYS HFSS) and experimental results. Considering the previous notch filter realized by SRRs [43], this research goal was to widen the bandstop by placing several notch frequencies of single SRRs close to each other so that it leads to a wide rejection band. In this regard, first, simulations were conducted. Second, fabrication of the structure and experiments were performed. Then, the equivalent circuit element parameters were obtained numerically from ANSYS HFSS. Finally, the theoretical transmission using the lumped elements was plotted using an ABCD transmission matrix approach.

3.1 Simulation

Simulations aid in overcoming the challenges associated with an iterative design, fabrication, and characterization cycle by predicting the performance in a relative short duration which enables the fabrication of THz circuits with an increased level of confidence. In this work ANSYS HFSS is used as a simulation tool to model the real devices and to calculate equivalent SRR lumped element parameters (R_r, L_r, C_r) to characterize the scattering parameters (S-parameters).

In Fig. 3. 1., a single SRR, illustrating the equivalent lumped circuit model of the single SRR, is presented where the resonant frequency is calculated from $f_{res} = 1/2\pi\sqrt{L_r C_r}$. By equation (2. 3), an approximate value for L_r is obtained, but there are no analytic expressions available for the SRR's capacitance on a thin substrate. Nevertheless, a full wave simulation for an arbitrary size of the SRR provides a resonant frequency and where the resultant electromagnetic fields are used to calculate L_r and C_r numerically. Again, according to (2. 3), by decreasing the radius of the SRR, the inductance of SRR decreases, which results in an increase in the resonant frequency (f_{res}), and vice versa.

Since there are no closed-form expressions available for the specific SRR geometry investigated in this work (i.e., SRR-coupled CPS on an ultra thin substrate), simulations were used to determine the appropriate size of single SRRs which will be discussed in the subsequent

sections. It must be highlighted that the validation of simulations was done with the experimental result in [43].

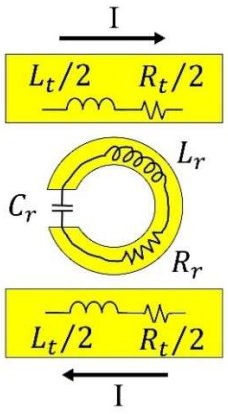

Fig. 3. 1. A single SRR, loaded to a CPS, demonstrating the equivalent circuit model of a single SRR. I is the current passing through the CPS. L_r, C_r, and R_r are the inductance, capacitance, and resistance of the single SRR, and L_t and R_t are the inductance and resistance of the CPS, respectively.

Fig. 3. 2 illustrates a unit cell of a single SRR-loaded CPS with wave port excitations. The left and right planes are wave ports, and the simulation domain is bounded by radiation boundaries. W, S, R_i, g, and C are the width of each line of the CPS, the separation between lines of the CPS, the inner radius of the single SRR, the split gap, and the width of the single SRR, respectively. The single SRR and TLs are gold mounted on Si_3N_4 substrate which is specified as purple. In simulations, the conductivity of gold (σ_{AU}) is $41\left(\frac{\mathrm{MS}}{\mathrm{m}}\right)$, relative permittivity (ϵ_{r}) and the loss tangent of Si_3N_4 are 7.6 and 0.00526, respectively.

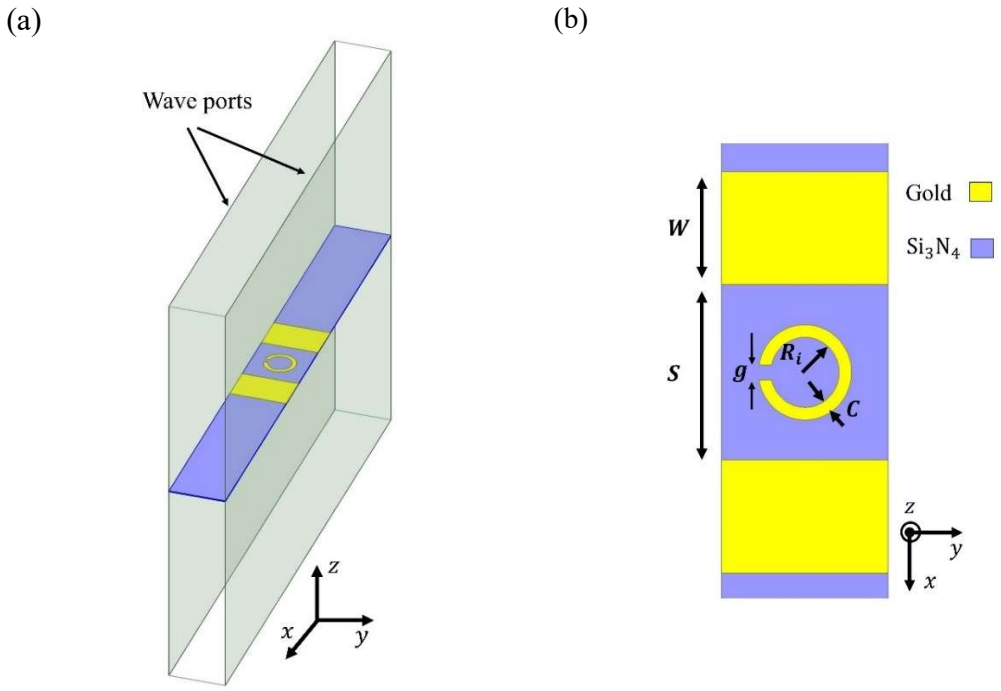

Fig. 3. 2. A unit cell of a single-SRR with boundaries. (a) 3D view. (b) 2D top view.

As mentioned, full-wave simulations were performed to obtain the S-parameters and electromagnetic fields that were used to calculate the lumped element circuit components. Fig. 3. 3 plots the simulated transmission of the structure shown in Fig. 3. 2 which has an inner radius of $R_i = 14$ µm. From simulation, the resonant frequency of this ring was found to be 1.06 THz and had an insertion loss of -6 dB at the center frequency. The simulated electric field distribution of the SRR is plotted in Fig. 3. 2 at two different frequencies 800 GHz (off resonance) and 1.06 THz (on resonance) in Fig. 3. 4, respectively. As it is seen, at the resonant frequency, the electric field is confined on the SRR. This happens because at the resonant frequency, the induced current on the ring is circulating with its maximum amplitude leading to a large charge to accumulate over the split gap. The energy of the travelling wave on the TL is transferred to the current on the ring, and the energy is dissipated on the ring due to the ohmic loss and radiation happening by the single SRR. In other words, the signal is attenuated at the resonant frequency.

Several varying sized resonant SRRs can be cascaded to broaden the stopband. In this regard, the CPS is loaded with SRRs with different radii. Three different radii of the single SRR are selected to be used: 13 µm (resonant frequency = 1.12 THz), 14 µm (resonant frequency = 1.06 THz), and 15 µm (resonant frequency = 0.975 THz). Frequency responses of these three SRR geometries (small, medium, large) are plotted in Fig. 3. 5(a).

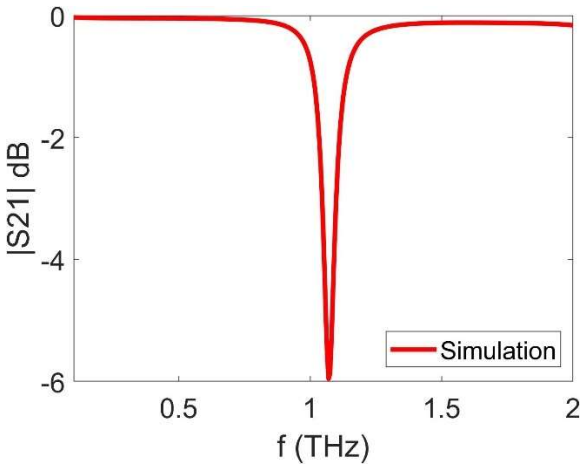

Fig. 3. 3. Frequency response of one medium size single SRR. R_i= 14 µm, C = 5 µm, g = 6 µm, W = 45 µm, and S = 70 µm.

(a) (b)

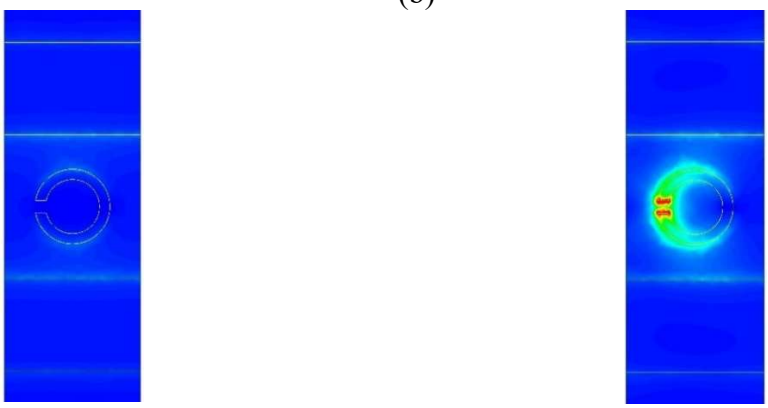

Fig. 3. 4. Electric field intensity over the single SRR depicted in Fig. 3. 2. (a) The frequency of the incident wave is 800 GHz (off resonance). (b) The frequency of the incident wave is 1.06 THz (on resonance).

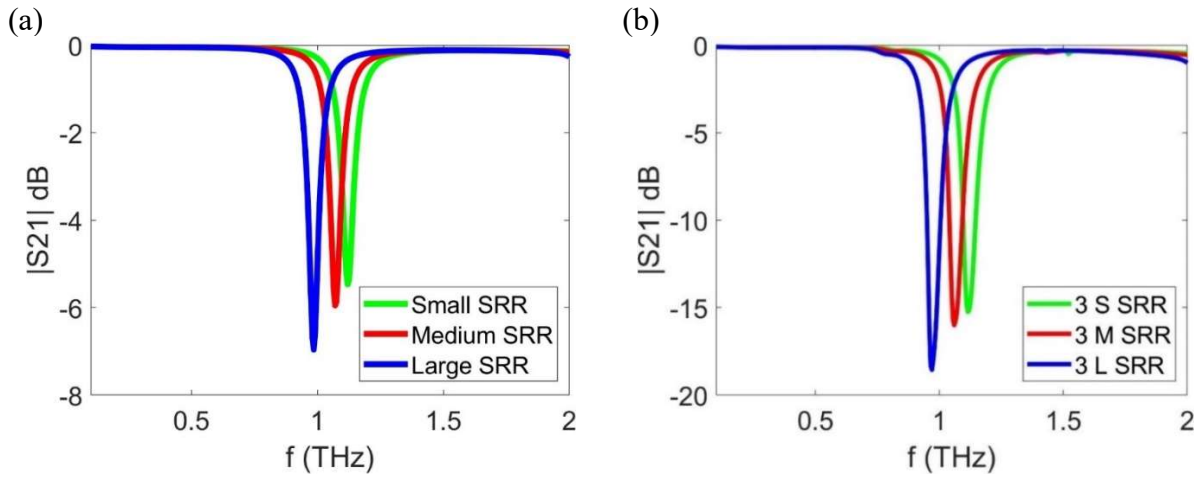

Fig. 3. 5. Frequency responses of a single SRR with radii of 13 μm (small), 14 μm (medium), and 15 μm (large), separately. (b) Frequency responses of groups of three small, three medium, and three large single SRRs corresponding to radii of 13 μm, 14 μm, and 15 μm, respectively.

The stopband attenuation of a single SRR ($\approx$ 6 dB) may be insufficient to construct a useful filter. A straightforward method to increase the attenuation is by cascading several SRRs of an identical radius. In Fig. 3. 5(b), we see the frequency responses of a group of three small SRR, three medium SRR, and three large SRR separately. The distance between SRRs is 30 μm. Comparing Fig. 3. 5(a) and Fig. 3. 5(b), the addition of more SRR of the same size increases the attenuation in the stopband from 6 dB up-to 16 dB.

In the next step, three small, three medium, and three large SRRs, in total nine SRRs are cascaded inside the CPS as shown in Fig. 3. 6(a). The S-parameter simulation of the CPS loaded with nine SRRs is provided in Fig. 3. 6(b). In this figure, $|S_{21}|^2 + |S_{11}|^2 < 1$, meaning that the filter is lossy which is due to radiative and ohmic losses. The simulation shows that a wide band-stop filter with center frequency around 1 THz is possible using a combination of cascaded SRRs. After designing the bandstop filter using simulations, characterizing the structure at THz frequencies using a modified THz-time-domain spectroscopy (TDS) setup was proceeded.

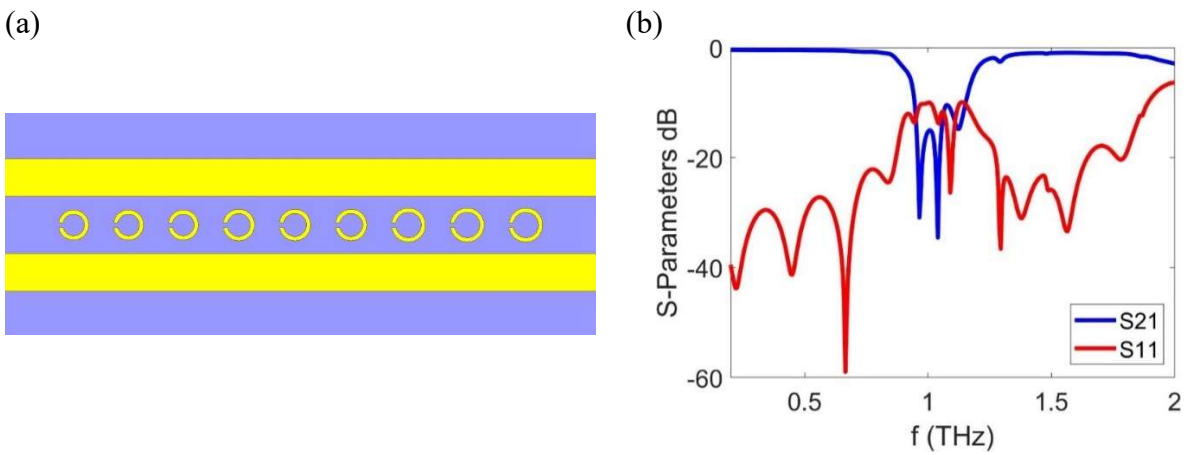

Fig. 3. 6. (a) Nine single SRRs composed of three small, three medium, and three large rings with Radii of 13 µm, 14 µm, and 15 µm, respectively. (b) The S-parameters response of nine SRRs loaded to the CPS.

3.2 Experimental results of loading nine SRRs to a CPS

In this section, the experimental results are presented. First, the nine single SRRs with biasing circuits is sillustrated in the AutoCAD layout which was used for fabrication. The AutoCAD layout of the structure including biasing circuits is depicted in Fig. 3. 7.

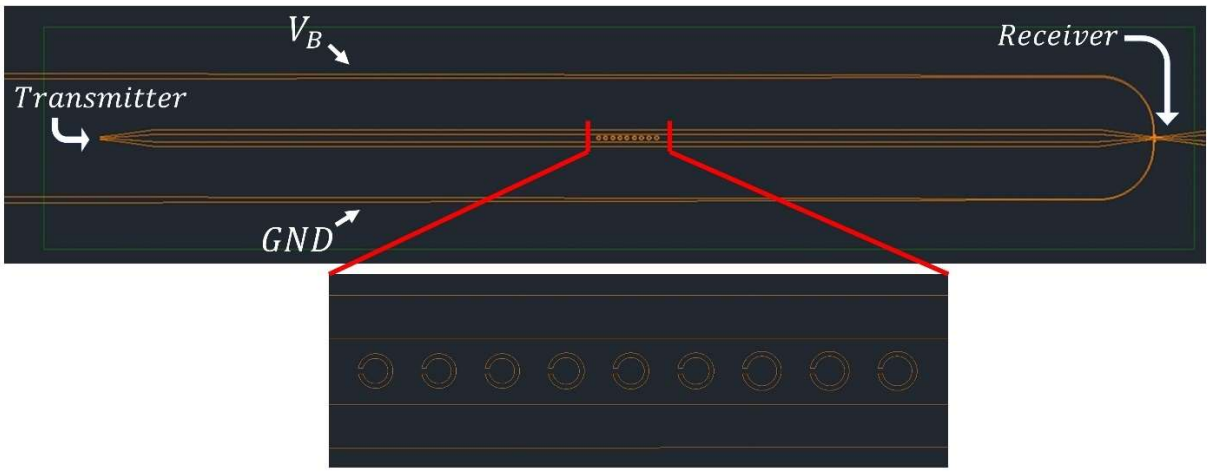

Fig. 3. 7. The layout designed in AutoCAD for fabrication.

The fabricated structure consists of three groups of three small, medium, and large SRRs loaded into a CPS with biasing circuit, a transmitter (Tx), and receiver (Rx) photoconductive switch (PCS) are illustrated in Fig. 3. 8(a). The distance between T_x and R_x is 1 cm, and single SRRs are placed in the middle of the CPS. The SRRs, CPS, and the biasing circuit are made of gold with 100 nm thickness which were deposited via RF sputtering. To enable THz-bandwidth pulse transmission, a thin 1 μm Si_3N_4 membrane is used as the substrate. If a thick substrate was used, then significant loss and dispersion would occur as discussed in section 1.2. The Tx PCS and Rx PCS are made of low-temperature grown gallium arsenide (LTG-GaAs) with size of 20 μm×40 μm×1.8 μm. The fabrication process is explained in [51]. Generation and detection of THz pulse are explained in Appendix A. Fig. 3. 8(a) shows a quarter of a wafer on which the filter structure in Fig. 3. 8(a) is fabricated. The Tx is connected to DC bias and the Rx is connected to a lock-in amplifier.

(a) (b)

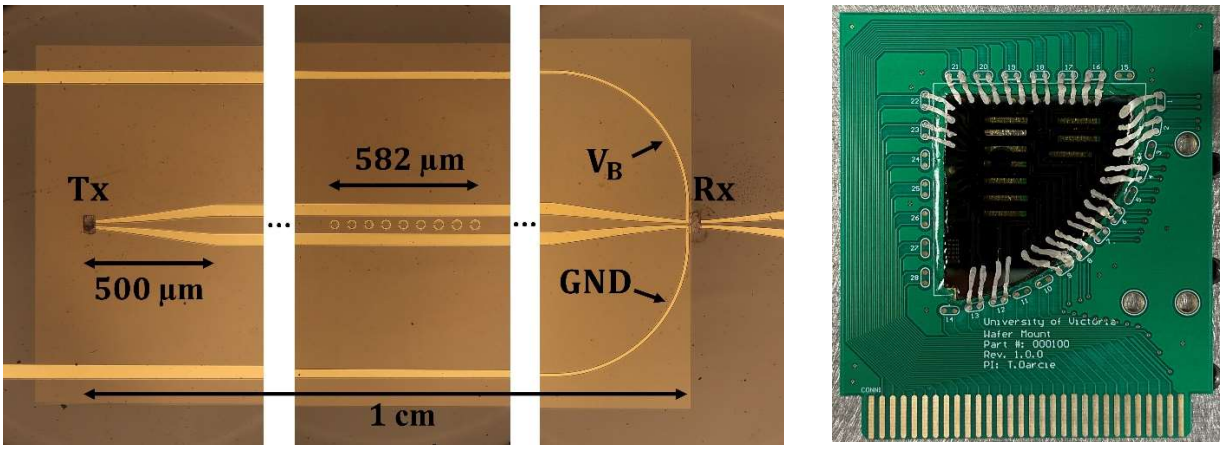

Fig. 3. 8. Fabricated nine single SRR with transmitter (Tx), receiver (Rx), biasing circuit, and the wafer. (a) Tx and Rx are LTG-GaAs photo-conductive switches. Transmission lines, SRR, and biasing connections are gold with 100 nm thickness. The membrane of the whole structure is $Si_3N_4$with 1 µm thickness. (b) The wafer on which the SRR filter in (a) is fabricated.

The experimental test setup is illustrated in Fig. 3. 9. A THz pulse is generated by illuminating an optical chopped signal onto the DC-biased Tx PCS. Next, the THz pulse propagates through the CPS until it is received at the Rx PCS. Meanwhile the THz pulse transmits through nine SRRs and experiences frequency-dependent attenuation arising from the cascaded single SRR bandstop filter. This setup illustrated in Fig. 3. 9 is a terahertz time-domain spectrometer (THz-TDS) which has been modified to enable for guided-wave analysis (compared to standard radiated waves). Standard THz-TDS is explained in more detail in appendix A.

(a) (b)

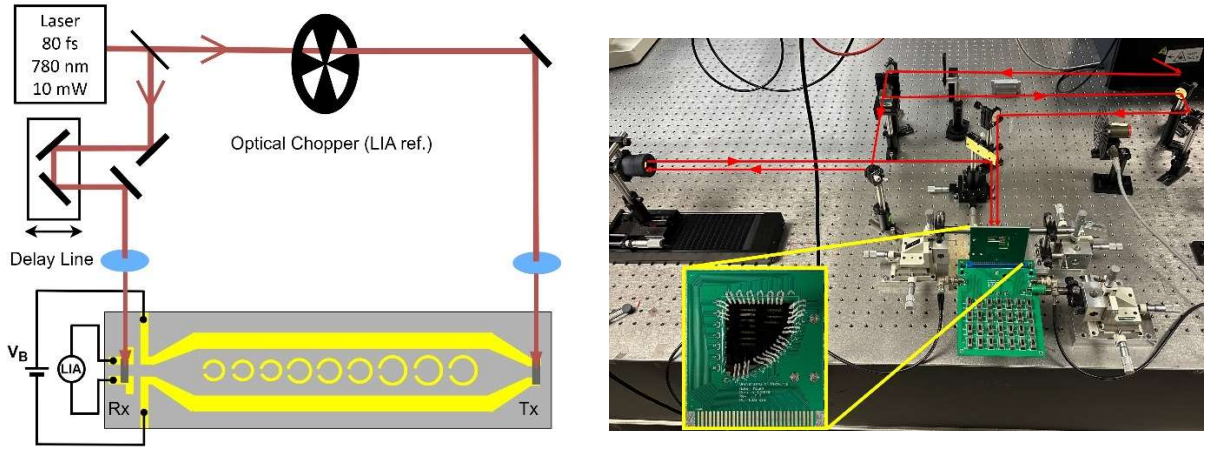

Fig. 3. 9. The set-up used to conduct the experiment. (a) Schematic and (b) implemented.

The simulation and experiment results of the normalized detected THz pulse in time domain are presented in Fig. 3. 10(a). In this figure, the black THz received pulse is the experiment result with FWHM of 1 ps, and the red THz pulse is the simulation. Concerning the simulation, the input time domain signal is a pulse with a rise and a fall time of 800 fs. The Fourier Transform of the time domain signal is shown in Fig. 3. 10(b) in which the vertical axis is the power of the detected THz signal. Since the time domain signal is in Gaussian shape, its Fourier Transform is Gaussian with a roll-off according to the time domain pulse width. The blue dashed curve is the Fourier Transform of an input simulated pulse fed to the CPS without SRRs. Hence, it is called reference so that we can compare the response of loaded CPS with SRRs with the reference response. In Fig. 3. 10(b), as it is seen, the filtering process causes attenuation of a range of frequency components. In this figure, the experimental SRRs' frequency response is made of three notch bandstop frequencies at 0.95 THz, 1.09 THz, and 1.12 THz which are close to the predicted values done by the frequency simulation in Fig. 3. 6(b). To visualize better, this figure is zoomed-in in Fig. 3. 11(a). It is also seen that at 1.23 THz, there is an attenuation deep. This is due to the higher order resonant frequency components and is seen in Fig. 3. 6(b) which is a full wave frequency simulation. Nonetheless, the Fourier Transform of the time domain simulation contains three notch bandstop responses which are close to the experimental result, showing a good compliance between simulations and experiment. The bandwidth of the filter for simulation and experiment is 0.32 THz and 0.36 THz, respectively.

Concerning the time domain response, Fig. 3. 10(a), a sine wave in one period is seen. This is because when the pico-second pulse arrives at Rx, due to not matched impedances, the wave reflects back toward Tx and by hitting SRRs, again due to difference in impedances, the wave

reflects toward Rx. This reflected wave is attenuated and dispersed so that, at Rx, it is received with smaller amplitude and wider FWHM. However, in the simulation boundary conditions, the wave ports are based on absorption boundary conditions which there is no reflection from the ports.

The roll-off in the Fourier Response continues until it reached to the noise floor of the experiment, meaning that the level of the signal is equal or less than the noise. The frequency at which the magnitude of the signal reaches to the noise floor is named cut-off frequency, and for this experiment the cut off frequency is about 1.9 THz, illustrated in Fig. 3. 11(b). As it is seen, the detection after the cut-off frequency is almost flat. This noise is originating from electronic components and connections like TL, probes, and electronic circuitry [52].

It is worth noting that the deviation of simulation from experiment is due to fabrication limitations and conditions which are not included in the simulation. Regarding fabrication, our lithography minimum feature size is almost 1 µm, which is close to the difference between radii of single SRRs (13 µm, 14 µm, and 15 µm). The impact of this limitation causes rounding of the SRR edge as it is seen in Fig. 3. 13. In addition, a difference between material parameters in the simulated and fabricated single SRR can cause the deviation between the simulation and experiment. Besides, noise and the environment temperature are not included in the simulation. Furthermore, the meshing condition and convergence error of the simulation were based on minimum values so the employed computer could process the simulation. These limitations have affected the simulation transient time domain results. Therefore, by cascading different size single SRRs corresponding to different notch bandstop frequencies, it is possible to make a wide bandstop filter.

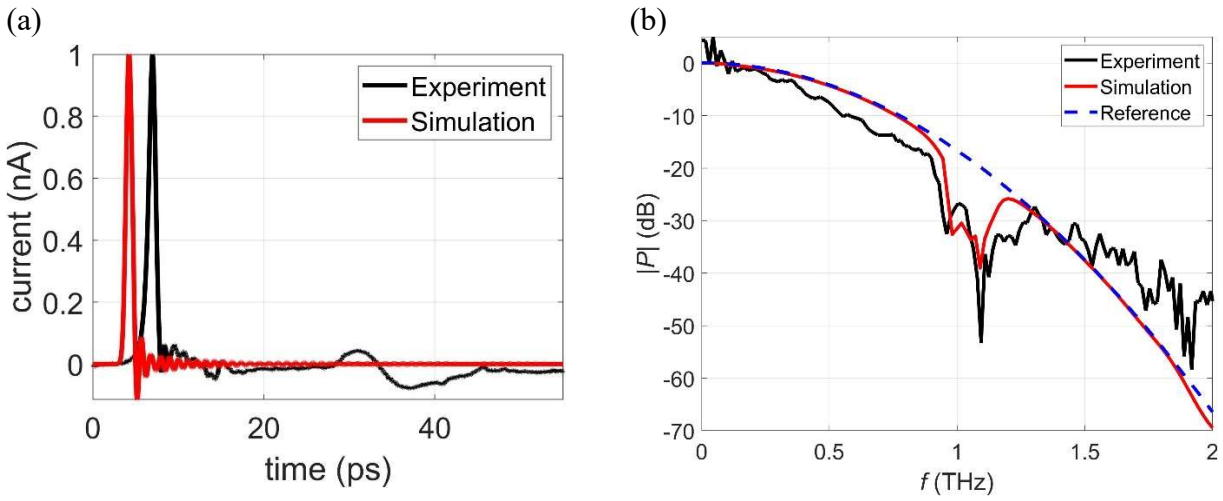

Fig. 3. 10. Experiment and simulation results of the CPS loaded with nine single SRRs bandstop filter. (a) time domain THz pulse at the receiver. (b) Fourier transform of the received THz pulse.

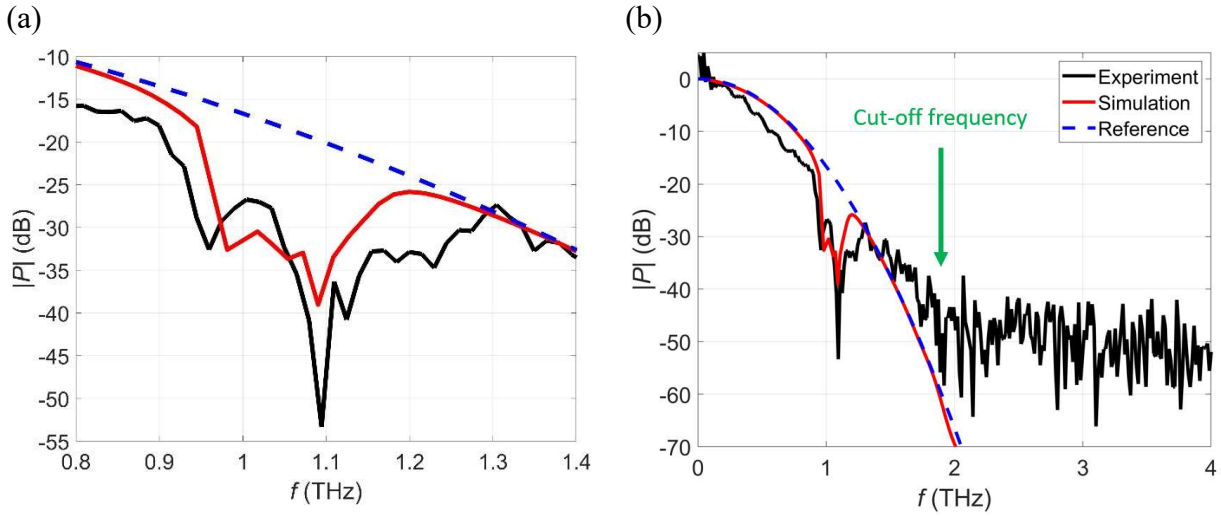

Fig. 3. 11. Reprint of Fig. 3. 11(b). (a) Zoom in. (b) The cut-off frequency in the Fourier Transform of the THz pulse.

After addressing the amplitude response, it is important to consider the phase response of the filter. As discussed in the first chapter, if the phase response is not a linear function of frequency, the output of the filter will be distorted. Therefore, sections of the frequency response that exhibit a linear phase response are of interest. Fig. 3. 12 illustrates the simulated phase response of the CPS loaded with nine single SRRs, alongside a reference simulated phase response (the phase response of the CPS alone) and the stopband markers.

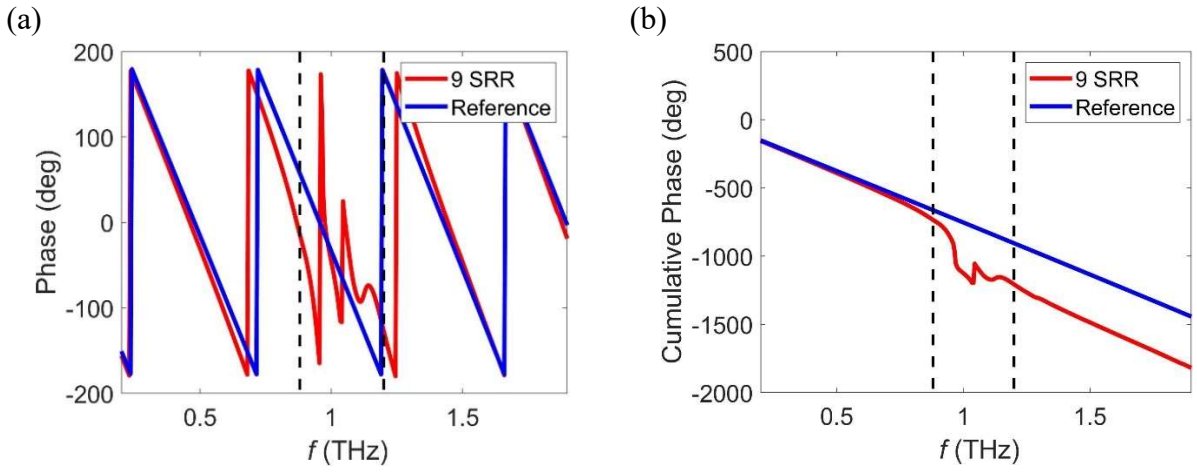

Fig. 3. 12. Simulated phase response of the CPS loaded with nine single SRRs bandstop filter. (a) Phase between -180 and 180 degrees. (b) Cumulative phase. Blue line is the response of the CPS alone (with no SRRs), and dashed lines are -3dB stopband markers from 0.88 THz to 1.2 THz.

According to this figure, over the stopband, the phase response (or phase shift) is non-linear. Nevertheless, since in the stopband the attenuation is high, the amplitude of the output is very small, and nonlinearity of the phase is not important. This non-linear phase shift is seen out of the stopband, starting from 0.7 THz to 1.3 THz. Except this region, the phase shift is linear. As a consequence, the non-linear phase response limits the bandpass region of this filter.

In the following section, the equivalent circuit model of the fabricated CPS loaded with nine single SRR is discussed.

3.3 Equivalent circuit of the fabricated CPS loaded with nine single SRRs bandstop filter

The bandstop filter investigated in this work can be modelled using lumped elements (for the SRRs) and distributed elements (for the transmission line between SRRs). A method to analyze this element combination is to use a cascade of ABCD matrices. A SRR unit section is shown in Fig. 3. 13. The equivalent lumped element circuit model of this section for each single SRR is obtained from simulation (ANSYS HFSS). Cascading these sections along with transmission lines provides the overall filter response. The equivalent circuit model of a single SRR section is illustrated in Fig. 3. 14. In this figure, $R_t, L_t, C_t, R_r, L_r, C_r,$ and M are CPS resistance, CPS inductance, CPS capacitance, SRR resistance, SRR inductance, SRR capacitance, and mutual inductance between CPS and SRR, respectively.

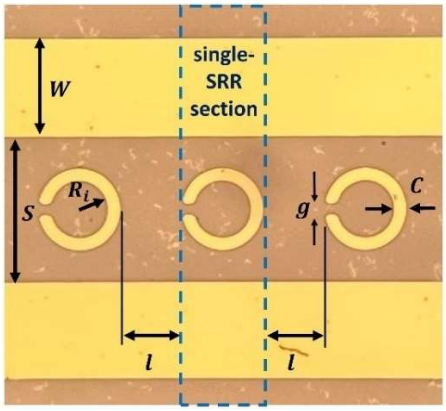

Fig. 3. 13. Dashed lines state the boundary of a single SRR section.

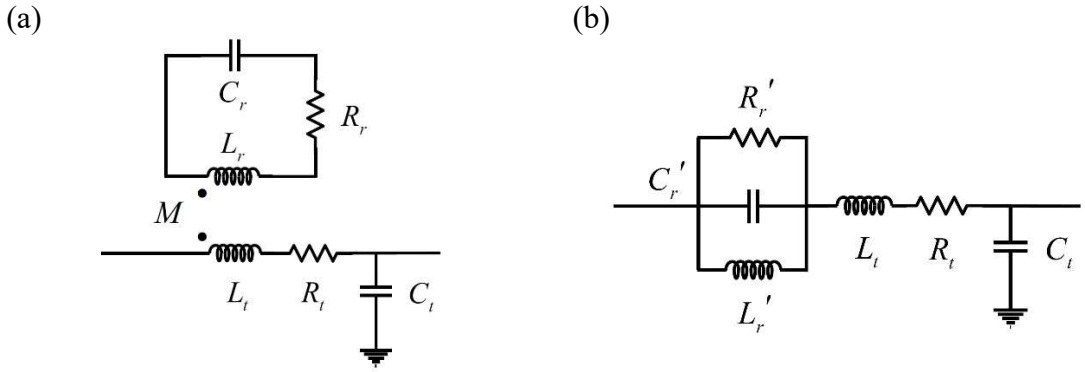

Fig. 3. 14. Equivalent circuit model for single SRR section. (a) There is a mutual inductance between single SRR and CPS. (b) the equivalent model of the circuit in (a).

To calculate the lumped element parameters of the circuit models illustrated in Fig. 3. 14, a full-wave simulation (in ANSYS HFSS) of the single SRR and CPS separately was performed. Then using the computed electric and magnetic field vectors, $\vec{E}(x,y,z)$ and $\vec{H}(x,y,z)$, the lumped element parameters were calculated [18]. The inductances, L_r and L_t, are obtained using (3. 1) where μ and I_0 are the permeability and total current passing through the element.

$$L = \frac{\mu}{|I_0|^2}\int_V \vec{H}\cdot\vec{H}^*\,dv \qquad \text{(H)}. \tag{3. 1}$$

A similar procedure is used to find capacitances of the TL and single SRR. The capacitances, C_r and C_t, are obtained using (3. 2) where ϵ and V_0 are the permittivity and total voltage [28]. V_0 is the total voltage on the TL and or single SRR separately, creating the electric field $\vec{E}$.

$$C = \frac{\epsilon}{|V_0|^2}\int_V \vec{E}\cdot\vec{E}^*\,dv \qquad \text{(F)}. \tag{3. 2}$$

The mutual inductance, *M*, between the TL and single SRR is calculated by (3. 3) where $\vec{B}$ is the magnetic flux density associated with the propagating electromagnetic wave, and S is the loop surface of the single SRR [15]. And the resonant frequency is given by (3. 4) [53]

$$M = \frac{\int_S \vec{B} \cdot ds}{I_0} \quad \text{(H)}, \tag{3. 3}$$

$$f_0 = \frac{1}{2\pi\sqrt{L_r C_r}} \quad \text{(Hz)}. \tag{3. 4}$$

The series resistance of rings and transmission line is calculated according to (3. 5). In this formula, R is ohms per meter, so it is multiplied by the length of TL or circumference of the single SRR to give the resistance of the specified length of TL or single SRR. C_1 and C_2 are integration path over conductor boundaries. R_S is the surface resistance of metal, ω, and σ are angular frequency and conductivity, respectively [18]. Lumped circuit elements (L_t, C_t, R_t, L_t, C_r, R_r, and M) are summarized in Table 3. 1. By circuit theory, the values of the equivalent circuit, Fig. 3. 14(b), are obtained from (3. 7) to (3. 10).

$$R = \frac{R_s}{|I_0|^2} \int_{C_1+C_2} \vec{H} \cdot \vec{H}^* dl \quad \text{(Ω/m)}, \tag{3. 5}$$

$$R_s = \sqrt{\omega\mu/2\sigma} \quad \text{(Ω)}. \tag{3. 6}$$

$$L_r' = C_r M^2 \omega^2 \quad \text{(H)}, \tag{3. 7}$$

$$C_r' = L_r / M^2 \omega^2 \quad \text{(F)}, \tag{3. 8}$$

$$R_r' = R_r / M^2 \omega^2 \quad \text{(Ω)}, \tag{3. 9}$$

$$\omega = 2\pi f \quad \text{(1/S)}. \tag{3. 10}$$

Table 3. 1. Lumped element values of the circuit model.

Single-SRR	C_r $[fF]$	L_r $[pH]$	R_r [Ω]	C_t $[fF]$	L_t $[pH]$	R_t [Ω]	M $[pH]$
Small	0.387	50.9	5.61	0.225	9	1.53	5.7
Medium	0.407	55.1	4.85	0.24	9.7	1.6	6.12
Large	0.43	62.4	2.77	0.27	11.3	1.7	7.24

Next, to verify the circuit model, which is obtained by lumped parameter values, the ABCD matrix approach [18] is applied to the cascaded nine single SRRs and the CPS between SRRs.

Then S21 responses based on ABCD matrix approach is compared to simulations. The ABCD matrix of a single SRR section is defined in (3. 11). Refer to appendix B for the definition and application of the ABCD matrix.

$$ABCD_{single-SRR} = \begin{bmatrix} 1 + Z_1/Z_2 & Z_1 \\ 1/Z_2 & 1 \end{bmatrix}, \tag{3. 11}$$

$$Z_1 = jL_t\omega + R_t + \frac{1}{jC_r'\omega - j/L_r'\omega + R_r'} \quad (\Omega), \tag{3. 12}$$

$$Z_2 = \frac{-j}{C_t'\omega} \quad (\Omega). \tag{3. 13}$$

The ABCD matrix for transmission line between single SRR sections is as follows in which c_0 is the speed of light, and $l = 30\mu m$ is the length of TL between single SRR sections.

$$ABCD_{TL} = \begin{bmatrix} \cos\left(\frac{\omega l}{c_0}\right) & jZ_0 \sin\left(\frac{\omega l}{c_0}\right) \\ jY_0 \sin\left(\frac{\omega l}{c_0}\right) & \cos\left(\frac{\omega l}{c_0}\right) \end{bmatrix} \tag{3. 14}$$

The response of the structure is a multiplication of ABCD matrices of single SRR sections and TLs. The BSF in this paper is constructed from three small, three medium, and three large rings. The response of the circuit model for three single SRR based on ABCD matrix is presented in (3. 15) and the ABCD matrix for total structure is presented in (3. 16). Finally, S_{21} response is calculated by (3. 17) in which Z_0 is characteristics impedance of CPS at both ends of nine single SRRs which is 210 ohms, extracted by simulation.

$$ABCD_{3SRR} = ABCD_{SRR} \times ABCD_{TL} \times ABCD_{SRR} \times ABCD_{TL} \times ABCD_{SRR} \tag{3. 15}$$

$$\begin{aligned} ABCD_{tot} = {} & ABCD_S \times ABCD_{TL} \times ABCD_S \times \cdots \\ & \times ABCD_M \times \cdots \times ABCD_{TL} \times ABCD_L \end{aligned} \tag{3. 16}$$

$$S_{21} = \frac{2}{A_{tot} + B_{tot}/Z_0 + C_{tot} \times Z_0 + D_{tot}} \tag{3. 17}$$

To examine the accuracy of the circuit model and the ABCD matrix approach, $|S_{21}|^2$ obtained by simulation and ABCD method for three single SRR are plotted in Fig. 3. 15. Solid lines (response by lumped circuit model) are close to the simulations. Nevertheless, the quality factor of the circuit model is higher than the simulation due to the radiation of energy by the ring at frequencies close to the resonant frequency, which is not considered in the lumped circuit model. The simulation and ABCD matrix results for the total structure containing nine single SRR are shown in Fig. 3. 16. The stopband of simulation is wider and stronger (attenuation) than the response of the circuit. Nevertheless, the circuit model provides a good approximation.

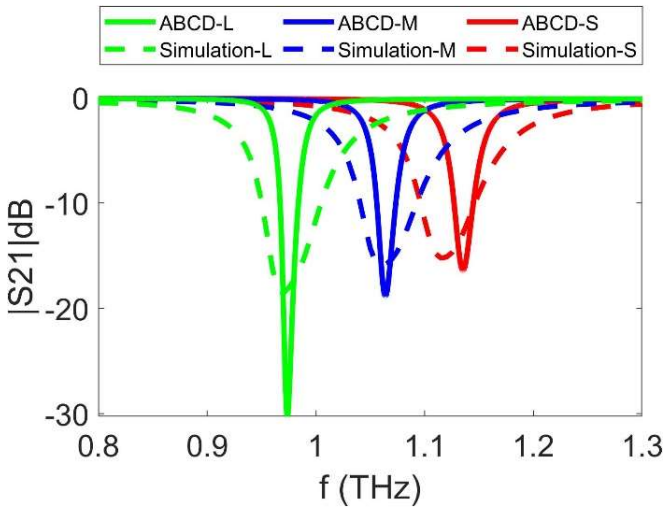

Fig. 3. 15. S21 response of a CPS loaded with three single SRRs obtained by simulation and ABCD matrix approach. Green, blue, and red are corresponded to rings with radius of 13 μm, 14 μm, and 15 μm, respectively.

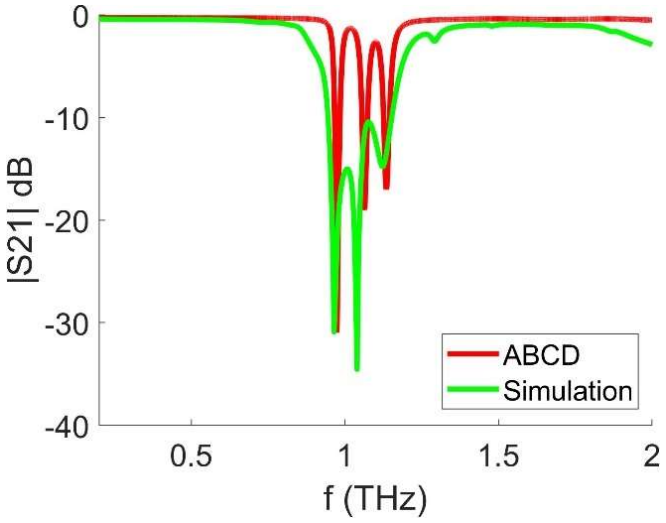

Fig. 3. 16. Simulation and ABCD approach Frequency response of the CPS loaded with nine single SRR with different radii of 13 µm, 14 µm, and 15 µm.

For comparison, in the following table, the work in this thesis is compared to some bandstop filters implemented by different types SRRs-loaded TL. In this table f_c and BW are the center frequency and bandwidth of the filter, respectively. As it is seen, the research in this thesis has resulted in a wider bandstop filter at a higher center frequency than the other ones. It should be emphasized that to the author's of this thesis knowledge, there is no wider bandstop filter made by TL loaded with SRRs over THz frequency range.

Table 3. 2. Examples of filters made by transmission lines loaded with SRR.

Ref.	Feedline	Resonator	f_c [GHz]	-3dB BW [GHz]
[36]	Coplanar waveguide	Double SRR	8	1.05
[42]	Coplanar stripline	Double SRR	5.4	0.5
[39]	Microstrip line	Double SRR & Complementary double SRR	1.3	0.08, 0.18
[54]	Microstrip line	Double SRR	6, 7, 8	0.1
[44]	Microstrip line	Double SRR	4.9	0.36
[55]	Goubau line	Double SRR	200-700	45
[56]	Goubau line	Double SRR	220-300	60
[43]	Coplanar stripline	Double SRR	500	60
This work	**Coplanar stripline**	**Single SRR**	**1000**	**360**

Therefore, considering results obtained from simulations and experiments, wide bandstop filters over THz frequency range can be realized by cascading notch filters based on SRRs of different radii.

Chapter 4

Contribution

Working on a project is a journey. Although this journey has a plan that aims to develop new and revolutionary ideas, it could also end an undesirable result. These undesirable results are still beneficial because it provides insight into previously unforeseen issues. In this chapter, the contribution that the research in this thesis has done to the THz group at the University of Victoria during my MASc program is presented.

4.1 General research contribution

Prior to the fabrication of the CPS loaded with nine single SRRs, it was necessary to do simulations due to the time and cost of experiments. Many simulations with different structures were performed to find a good structure for bandstop and bandpass filters in the THz range (from 0.1 THz to 2 THz) according to the sensitivity of the instruments in the THz group's lab. The simulations investigated:

- Changing the radii of single SRRs and single SSRs (split-square resonators) loaded to CPS to increase the stop band filters. The results of simulation related to the single SRRs are provided in the results chapter which based on those, we decided to fabricate the filter. The results of simulations of SSRs were very similar to SRRs' results, but unfortunately, the fabricated samples containing single SSRs were all defective so that the wise decision was to stick to SRRs.
- Loading CPS with SRRs and SSRs in order to make a bandpass filter in THz. Many different structures were simulated. In some cases, optimistic results in the passband were obtained which needed to be stronger. Nevertheless, a desirable structure was not found in my endeavors. These results will save the time of researchers, in THz group, who want to create bandpass filters based on SRRs and SSRs.
- Using rectangular rods in conjunction with CPS to make bandstop and or bandpass filters. The resonance response of the filter was obtained, but at frequencies a little higher than resonance the response was not suitable. Definitely, more simulation is required for this aim. These simulations will save time of future students in THz group.

4.2 Scientific literature contribution

An article named “Terahertz Bandstop Filter Using Varying Radii Split-Ring Resonators,” is submitted to IEEE Transactions on Terahertz Science and Technology. This article presents the results reported in the results and discussion chapter.

Chapter 5

Conclusion and Future Work

In this chapter, a conclusion of the thesis is provided, and then subjects for future works are suggested.

5.1 Conclusion

This thesis focused on the design, fabrication, and experimental characterization of a bandstop filter with center frequency at 1 THz constructed from nine single SRRs inside a CPS. The filter is composed of nine single SRRs in three groups of three single SRRs. Each group has a slightly different radii that results in three different resonant frequencies that when cascaded result in a broader rejection band. The radii of rings are 13 μm, 14 μm, and 15 μm corresponding to resonant frequencies 1.12 THz, 1.06 THz, and 0.975 THz, respectively. After simulating with ANSYS HFSS, the filter was fabricated on a 1 μm membrane of Si_3N_4. The bandwidth of the fabricated filter is 360 GHz. The result of the simulation was in a good agreement with the experiment. Next, the equivalent lumped element circuit model of the filter was obtained numerically in ANSYS HFSS. The response of the circuit model was obtained by the ABCD matrix approach which follows the simulation. This thesis is a continuation of previous works on notch filters. Lastly, I note that while SRRs are commonly used as an 'atom' in a metamaterial, this work focused on their application as a sub-wavelength filtering element.

5.2 Future work

Lots of work has been performed on different transmission lines loaded with SRRs over different ranges of frequencies. The work in this thesis was conducted specifically for frequencies about 1 THz and was limited to the single SRR geometry. Without any doubt, different structures composed of different materials lead to desirable responses over wanted frequency ranges. The following subjects can be possible continuation of this thesis and considered for possible future works:

- Using different geometry for SRRs in bandstop filters. The coupling between transmission line and SRRs is magnetic and electric with different strengths. Different geometries have different strengths of coupling resulting in wider or smaller bandwidth of a filter.
- Employing rods in shunt or series with transmission line. Rods behave like a series capacitor and inductor, so it has a resonant frequency. The coupling between rods and transmission lines is electric, and instead of the permeability, the permittivity becomes negative. Inserting rods can results in different strength of coupling between transmission line and rod which is desirable considering the goals.
- Loading both SRRs and rods to transmission lines. This combination contains negative permeability and permittivity leading to negative refractive index. The latter causes backward wave propagation in the medium.
- Applying SRRs and/or rods to transmission lines to create bandpass filters. Bandpass filters are of necessary components of high frequency circuits. The coupling between a transmission line and SRRs and or rods may be helpful in making an electrical connection at resonant frequency between two separated pieces of transmission lines, then results in a realization of a bandpass filter.
- Designing tunable SRR or rod to have tunable filters. By exploiting MEMS technology, it is possible to design filters that their resonant frequencies move and are controlled by external voltage or current.

Appendix A

Broadband THz generation, detection, and experimental spectroscopy

A.1 Broadband THz generation

Terahertz waves are generated either by accelerating electrons or by illuminating electromagnetic waves on nonlinear media. In the latter case, the incident waves undergo frequency conversion, up or down conversion. The output THz wave can be broadband or continuous [2]. Each of THz generation technique employs different approaches. Among them opto-conductivity (related to electron acceleration) and optical nonlinearity (using nonlinear media) are generally used. Photoconductivity is broadly used due to its simplicity, compactness, and ability of connecting to fiber optics [57]. In addition, the output THz signal of the photoconductive system can be broadband or continuous THz wave if the input excitation is a femtosecond laser or an optical beat, respectively [2]. In this thesis, experiments were conducted based on the photoconductivity approach to do the study in a wide range of frequency in THz region (from 0.1 THz to 2 THz). Hence, in this section, the generation of broadband THz waves based on the photoconductive method is discussed.

In Fig. A. 1, the process of creating a broadband THz wave by shining a femtosecond laser on a biased photoconductive antenna is depicted.

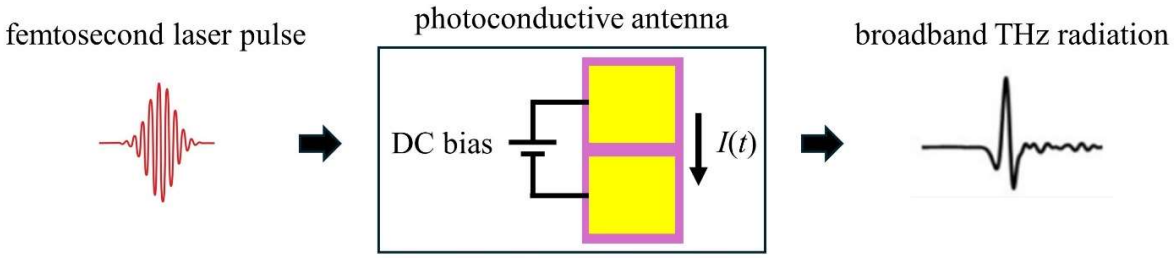

Fig. A. 1. Creating a broadband THz wave by shining a femtosecond laser on a biased photoconductive antenna [2].

A photoconductive antenna consists of a semiconductor substrate and two metallic connections (usually gold) deposited on the substrate. When light shines on the substrate, electron-hole pairs are created, increasing the conductivity of the substrate. Then by applying an electric field, typically a DC voltage in the transmitter, an electric current flows through the metallic conductors. Because of this, photoconductive antenna is also called a photoconductive switch as it behaves like a switch working with light. In addition, accelerating electrons (current) results in emitting electromagnetic wave from the structure, so this component is called photoconductive antenna. Fig. A. 2 shows a photoconductive antenna.

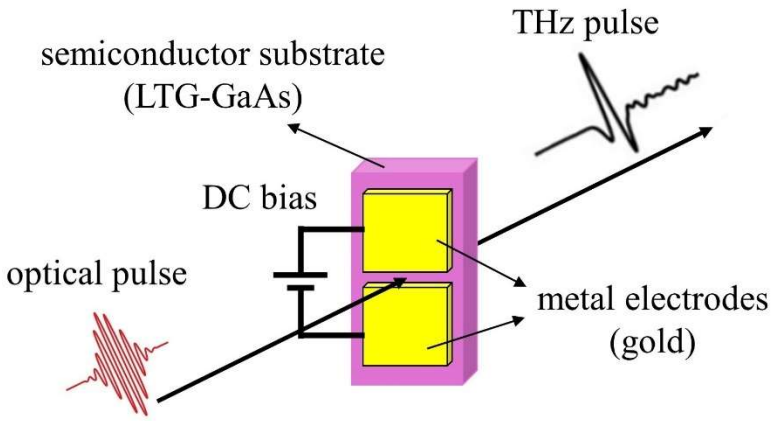

Fig. A. 2. A Biased Photoconductive antenna [2].

To have a broad THz wave, the duration of the emitted electromagnetic wave (which is switch-on plus switch-off times) should be sub-picosecond. The switch-on and switch-off times result from the optical pulse width and carrier lifetime of the substrate semiconductor, respectively. Thus, a short laser pulse (femtosecond laser) and short carrier (electron and hole) lifetime, 1 ps or less, in substrate are necessary. Low temperature grown GaAs (LTG-GaAs) has a carrier lifetime of 0.2 ps due to the high concentration of defects, making it a suitable candidate for photoconductive antennas.

A.2 Broadband THz detection

Similar to the THz generation, there are different techniques to detect THz waves among which the photoconductive antenna is simple and compact for detecting the amplitude of THz waves in time. Fig. A. 3 illustrates the underlying detection of THz waves based on the photoconductive antenna method [2]. In this method, the photoconductive antenna is not biased, and both THz and optical pulses are incident to the photoconductive antenna. The optical pulse creates electron-holes

pairs (photocarriers) in the semiconductor substrate of the photoconductive antenna. Then the electric field of the THz waves causes the photocarriers to move. This current is proportional to the amplitude of the incident THz wave. Consequently, the shape of the incident THz wave is mapped as a photocurrent signal in time, passing through the photoconductive antenna, by changing the time delay between the THz wave and optical pulse. To detect THz waves, the lifetime of carriers must be smaller than the THz pulse duration, so LTG-GaAs is a good candidate for this operation. In Fig. A. 4, a photoconductive antenna with the incident THz and optical waves are depicted. The photocurrent is in the order of nanoampere, so a current amplifier is required for amplification [2].

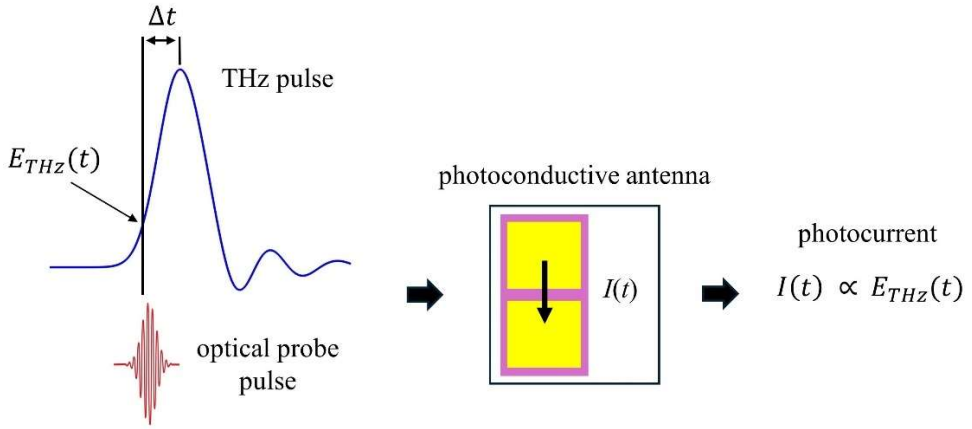

Fig. A. 3. Detection of a broadband THz wave with a photoconductive antenna [2].

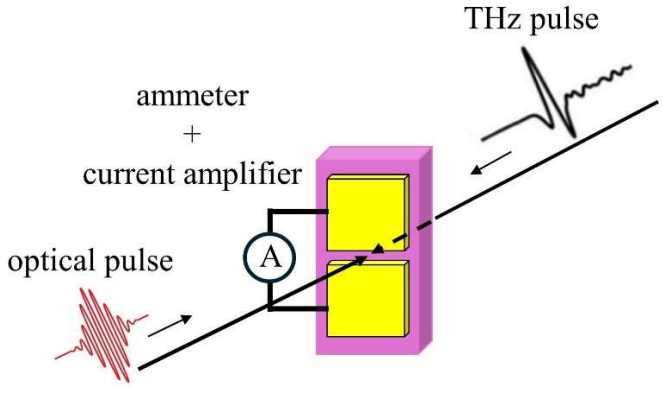

Fig. A. 4. Photoconductive antenna as a receiver to detect THz waves [2].

In Fig. A. 5, the measured electric fields of a THz wave and numerically simulated electric fields of a laser (50 fs at 800 nm), which has created the THz pulse, are shown in the time domain. The optical pulse is in the form of a Gaussian pulse overlying a sinusoidal carrier wave. The detection phenomenon of a THz wave is illustrated in Fig. A. 6. As discussed above, the electric field of the incident THz wave is mapped as an output current. Hence, in this figure, the electric field of the THz wave which is meant to be detected (or the output current) is shown in (d), and in figures (a), (b), and (c) this THz wave and the optical pulse (femtosecond lase) are approaching to the photoconductive antenna from right and left, respectively. In addition, the receiver (detector) photoconductive antenna is shown in its side view. In figure (d), the x-axis is the time difference (Δt) between the optical pulse and the received THz pulse at the detector. At point t_A, the THz wave has not yet reached to the photoconductive antenna, so there is no electric field and no current. At t_B and t_C, the optical pulse arrives at the photoconductive antenna with the positive peak and negative peak of the THz wave, respectively, which result in currents passing through the photoconductive antenna according to the electric field of the incident THz wave. Therefore, the detection of the THz wave in time domain is carried out by varying the delay between optical pulse (laser) and the incident THz pulse at the detector photoconductive antenna [58].

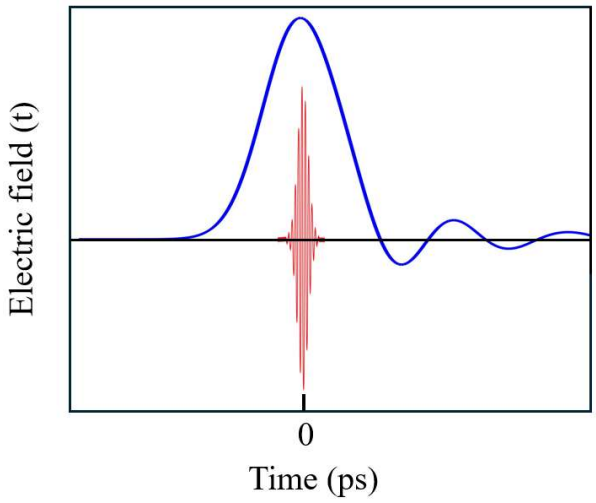

Fig. A. 5. Electric fields of THz and laser signals in time domain [58].

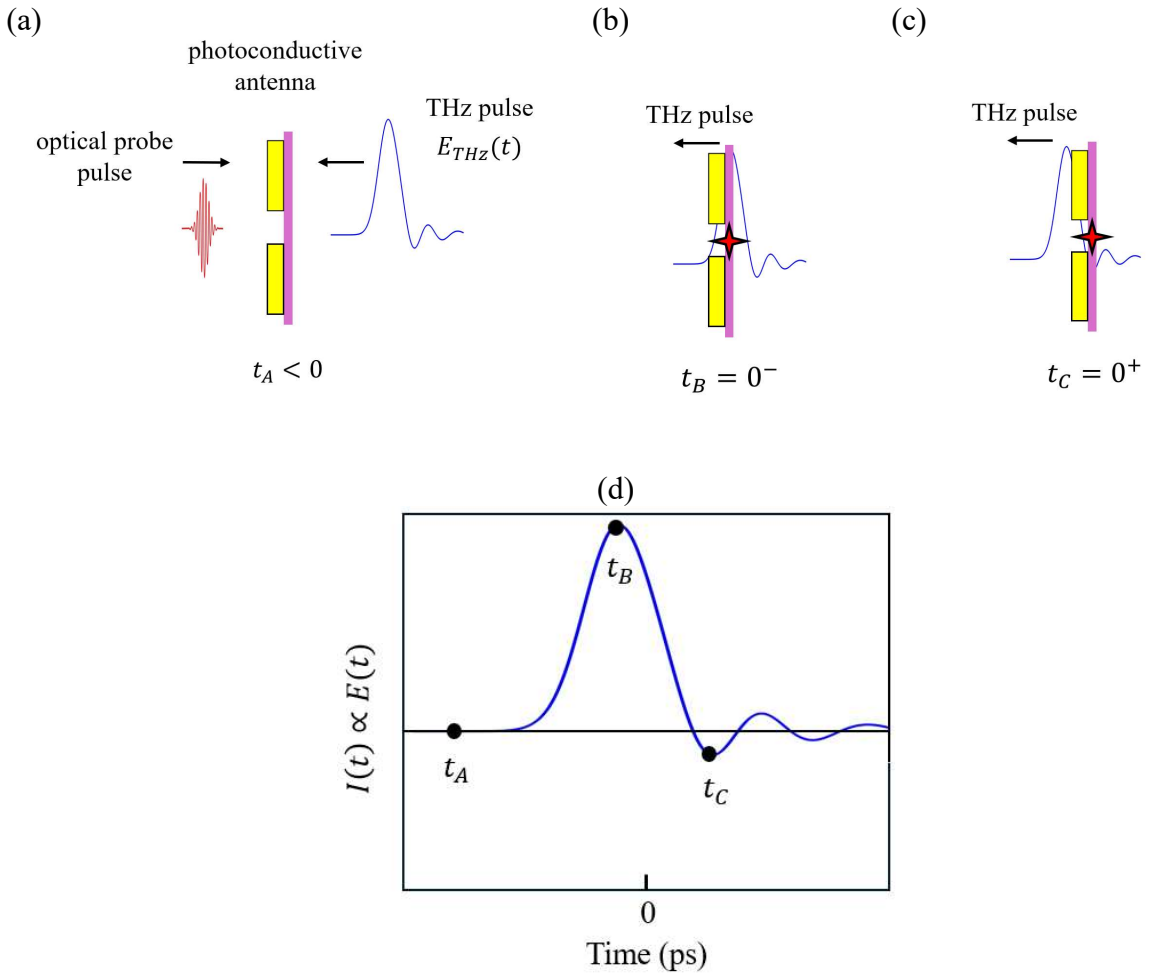

Fig. A. 6. Detection process of a THz wave. (a)-(c) Delay between arrival of the optical pulse (left wave) and the electric field of a THz pulse (right wave). (d) An incident THz pulse, $E(t)$, or detected output current, $I(t)$ [58].

A.2 Broadband THz experimental time-domain spectroscopy

Generation and detection of THz pulses based on photoconductive antenna were discussed in the two previous sections. In this section, the experimental setup used to generate and detect THz waves affected by samples is presented. Fig. A. 7 illustrates the setup used for THz standard spectroscopy. The laser pulse is divided into two beams by the beamsplitter: one beam generates the THz wave at the transmitter (or source) and the other beam detects the THz wave at the receiver (or detector). The optical pulse which is shined on the transmitter passes through a delay line. This delay line is necessary to make delay time (Δt) which is required to map (detect) THz pulse at the receiver photoconductive antenna, as discussed in section A.2. To successfully detect the THz wave, it is important that the THz wave and optical pulse arrive at the receiver simultaneously, as

mentioned in the previous section. For this, the delay line ensures that the path length from the beamsplitter to the receiver in the generation part is equal to the path length from the beamsplitter to the receiver in the detection part. The delay line can be used either in the generation or the receiver path [58].

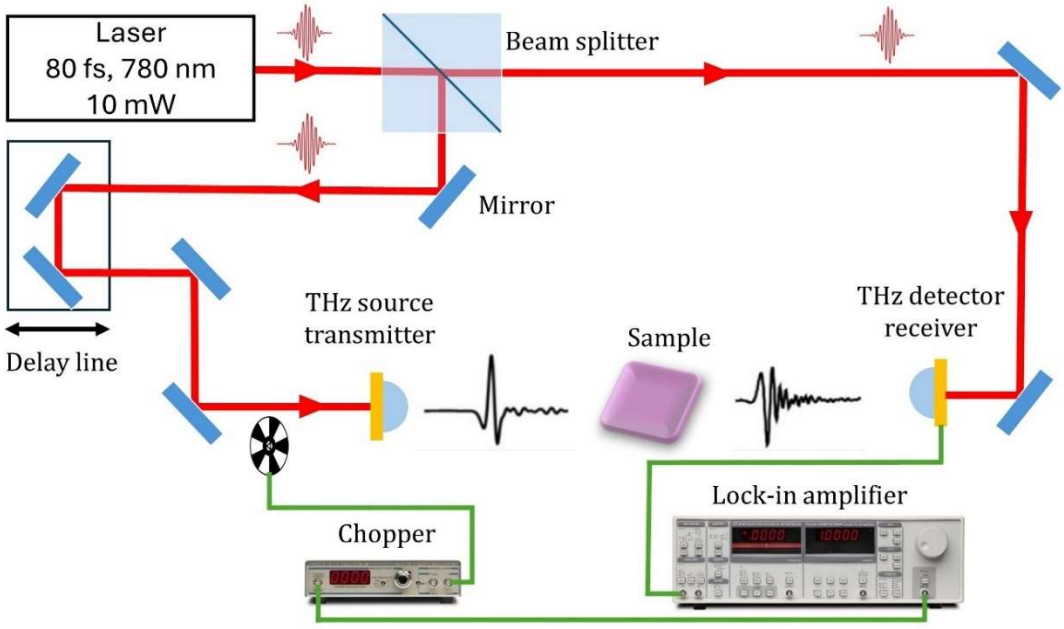

Fig. A. 7. An experimental set-up used for THz time domain spectroscopy.

In Fig. A. 7, a combination of a lock-in amplifier and a chopper is used to detect very low-level signals. A modulation is applied to the light source then the desired signal is recovered at the modulated frequency. The chopper continuously cuts the optical signal causing a modulation in the optical signal. In addition to modulating the optical signal, the copper provides a reference signal for the lock-in amplifier. The lock-in amplifier measures the detected signal at the reference frequency and rejects noise or other signals with different frequencies. Therefore, the lock-in amplifier enables clear detection of very small signals [59].

Appendix B

ABCD Matrix

ABCD matrix is a transmission matrix used to describe the relationship between the input and the output of two-port networks, Fig. B. 1, as follows:

$$\begin{bmatrix} V_1 \\ I_1 \end{bmatrix} = \begin{bmatrix} A & B \\ C & D \end{bmatrix} \begin{bmatrix} V_2 \\ I_2 \end{bmatrix} \tag{B. 1}$$

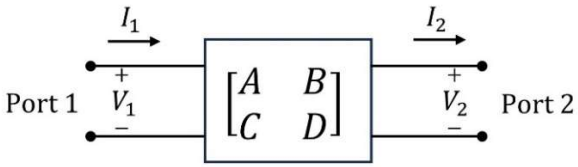

Fig. B. 1. A two port network and the transmission ABCD matrix [18].

When several two-port networks are cascaded, the total transmission matrix is the multiplication of the ABCD matrix of each two-port network. Fig. B. 2 illustrates a cascade connection of two two-port networks. The ABCD matrix of each individual network in this figure is formulated in (B. 2) and (B. 3). By substituting (B. 2) in (B. 3), the total ABCD matrix of this network is obtained as the product of the ABCD matrix of each individual two-port networks, as depicted in (B. 4).

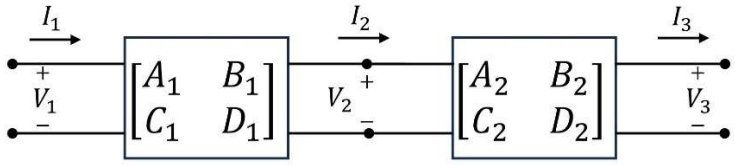

Fig. B. 2. A network consists of a cascade connection of two two-port networks [18].

$$\begin{bmatrix} V_1 \\ I_1 \end{bmatrix} = \begin{bmatrix} A_1 & B_1 \\ C_1 & D_1 \end{bmatrix} \begin{bmatrix} V_2 \\ I_2 \end{bmatrix} \quad \text{(B. 2)}$$

$$\begin{bmatrix} V_2 \\ I_2 \end{bmatrix} = \begin{bmatrix} A_2 & B_2 \\ C_2 & D_2 \end{bmatrix} \begin{bmatrix} V_3 \\ I_3 \end{bmatrix} \quad \text{(B. 3)}$$

$$\begin{bmatrix} V_1 \\ I_1 \end{bmatrix} = \begin{bmatrix} A_1 & B_1 \\ C_1 & D_1 \end{bmatrix} \begin{bmatrix} A_2 & B_2 \\ C_2 & D_2 \end{bmatrix} \begin{bmatrix} V_3 \\ I_3 \end{bmatrix} \quad \text{(B. 4)}$$

Since matrix multiplication is not commutative in general, the order of the ABCD matrix multiplication must follow the order of the two-port networks.

After finding the ABCD matrix of a two-port network, it is possible—and indeed the convenient way—to calculate S, Z, and Y matrices. Since S-parameters play an important role in the transfer function of networks, S-parameters are provided based on the ABCD parameters from (B. 5) to (B. 8). Z_o is the impedance connected to the out put of the two-port network, Fig. B. 3. A network terminated to the load impedance Z_o. In other words, Z_o is the last impedance that the cascaded networks are terminated to [18].

$$\mathrm{S11} = \frac{A + B/Z_o - CZ_o - D}{A + B/Z_o + CZ_o + D} \quad \text{(B. 5)}$$

$$\mathrm{S12} = \frac{2(AD - BC)}{A + B/Z_o + CZ_o + D} \quad \text{(B. 6)}$$

$$\mathrm{S21} = \frac{2}{A + B/Z_o + CZ_o + D} \quad \text{(B. 7)}$$

$$\mathrm{S22} = \frac{-A + B/Z_o - CZ_o + D}{A + B/Z_o + CZ_o + D} \quad \text{(B. 8)}$$

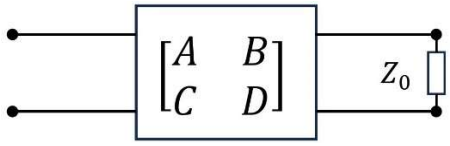

Fig. B. 3. A network terminated to the load impedance Z_o.

Bibliography

References

[1] W. Withayachumnankul and D. Abbott, “Metamaterials in the Terahertz Regime,” *IEEE Photonics J.*, vol. 1, no. 2, pp. 99–118, Aug. 2009, doi: 10.1109/JPHOT.2009.2026288.

[2] Y. Lee, *Principles of Terahertz Science and Technology*. Boston, MA: Springer US, 2009. doi: 10.1007/978-0-387-09540-0.

[3] H. Chen *et al.*, “High-sensitivity in vivo THz transmission imaging of early human breast cancer in a subcutaneous xenograft mouse model,” *Opt. Express*, vol. 19, no. 22, p. 21552, Oct. 2011, doi: 10.1364/OE.19.021552.

[4] H.-B. Liu, H. Zhong, N. Karpowicz, Y. Chen, and X.-C. Zhang, “Terahertz Spectroscopy and Imaging for Defense and Security Applications,” *Proc. IEEE*, vol. 95, no. 8, pp. 1514–1527, Aug. 2007, doi: 10.1109/JPROC.2007.898903.

[5] J. Qin, Y. Ying, and L. Xie, “The Detection of Agricultural Products and Food Using Terahertz Spectroscopy: A Review,” *Appl. Spectrosc. Rev.*, vol. 48, no. 6, pp. 439–457, Aug. 2013, doi: 10.1080/05704928.2012.745418.

[6] D. S. Sitnikov, S. A. Romashevskiy, A. A. Pronkin, and I. V. Ilina, “Open-path gas detection using terahertz time-domain spectroscopy,” *J. Phys. Conf. Ser.*, vol. 1147, p. 012061, Jan. 2019, doi: 10.1088/1742-6596/1147/1/012061.

[7] T. Nagatsuma, G. Ducournau, and C. C. Renaud, “Advances in terahertz communications accelerated by photonics,” *Nat. Photonics*, vol. 10, no. 6, pp. 371–379, Jun. 2016, doi: 10.1038/nphoton.2016.65.

[8] D. H. Auston and M. C. Nuss, “Electrooptical generation and detection of femtosecond electrical transients,” *IEEE J. Quantum Electron.*, vol. 24, no. 2, pp. 184–197, Feb. 1988, doi: 10.1109/3.114.

[9] J. He, X. He, T. Dong, S. Wang, M. Fu, and Y. Zhang, “Recent progress and applications of terahertz metamaterials,” *J. Phys. Appl. Phys.*, vol. 55, no. 12, p. 123002, Mar. 2022, doi: 10.1088/1361-6463/ac3282.

[10] F. Martín, *Artificial Transmission Lines for RF and Microwave Applications*, 1st ed. Wiley, 2015. doi: 10.1002/9781119058403.

[11] K.C. Gupta, Ramesh Garg, Inder Bahl, and Prakash Bhartia, *Microstrip Lines and Slotlines*, 2nd ed. Norwood, MA: Artech House, 1996.

[12] M. E. Holda, G. E. Ponchak, and E. M. Tentzeris, “Coplanar Stripline Single Pole Single Throw Switch,” *IEEE Microw. Wirel. Technol. Lett.*, vol. 33, no. 6, pp. 671–674, Jun. 2023, doi: 10.1109/LMWT.2023.3240658.

[13] H.-H. Lin, H.-K. Chiou, and C.-Y. Chang, “Balun design for uniplanar broad band double balanced mixer,” *Electron. Lett.*, vol. 31, no. 24, pp. 2113–2114, Nov. 1995, doi: 10.1049/el:19951404.

[14] A. Nesic, V. Trifunovic, and B. Jokanovic, “Highly Efficient Two-Dimensional Printed Antenna Array with a New Feeding Network,” in *14th European Microwave Conference, 1984*, Liege, Belgium: IEEE, Oct. 1984, pp. 697–701. doi: 10.1109/EUMA.1984.333423.

[15] F. T. Ulaby and U. Ravaioli, *Fundamentals of applied electromagnetics*, Eighth edition. Hoboken, NJ: Pearson, 2020.
[16] M. Y. Frankel, S. Gupta, J. A. Valdmanis, and G. A. Mourou, "Terahertz attenuation and dispersion characteristics of coplanar transmission lines," *IEEE Trans. Microw. Theory Tech.*, vol. 39, no. 6, pp. 910–916, Jun. 1991, doi: 10.1109/22.81658.
[17] D. P. Kasilingam and D. B. Rutledge, "Surface-Wave Losses of Coplanar Transmission Lines," in *MTT-S International Microwave Symposium Digest*, Boston, Mass, USA: MTT005, 1983, pp. 113–116. doi: 10.1109/MWSYM.1983.1130827.
[18] D. M. Pozar, *Microwave engineering*, Fourth Edition. Hoboken, NJ: John Wiley & Sons, Inc, 2012.
[19] M. Steer, *Fundamentals of Microwave and RF Design*. Raleigh, North Carolina: North Carolina State University Libraries, 2019.
[20] H. Cheng, J. F. Whitaker, T. M. Weller, and L. P. B. Katehi, "Terahertz-bandwidth pulse propagation on a coplanar stripline fabricated on a thin membrane," *IEEE Microw. Guid. Wave Lett.*, vol. 4, no. 3, pp. 89–91, Mar. 1994, doi: 10.1109/75.275590.
[21] W. Zhang, E. R. Brown, M. Rahman, and M. L. Norton, "Observation of terahertz absorption signatures in microliter DNA solutions," *Appl. Phys. Lett.*, vol. 102, no. 2, p. 023701, Jan. 2013, doi: 10.1063/1.4775696.
[22] M. R. Kutteruf, C. M. Brown, L. K. Iwaki, M. B. Campbell, T. M. Korter, and E. J. Heilweil, "Terahertz spectroscopy of short-chain polypeptides," *Chem. Phys. Lett.*, vol. 375, no. 3–4, pp. 337–343, Jul. 2003, doi: 10.1016/S0009-2614(03)00856-X.
[23] C. S. Joseph *et al.*, "Terahertz spectroscopy of intrinsic biomarkers for non-melanoma skin cancer," presented at the SPIE OPTO: Integrated Optoelectronic Devices, K. J. Linden, L. P. Sadwick, and C. M. O'Sullivan, Eds., San Jose, CA, Feb. 2009, p. 72150I. doi: 10.1117/12.809402.
[24] D. Natarajan, *A Practical Design of Lumped, Semi-lumped & Microwave Cavity Filters*, vol. 183. in Lecture Notes in Electrical Engineering, Berlin, Heidelberg: Springer Berlin Heidelberg, 2013. doi: 10.1007/978-3-642-32861-9.
[25] A. V. Oppenheim, A. S. Willsky, and S. H. Nawab, *Signals & systems*, 2nd ed. in Prentice-Hall signal processing series. Upper Saddle River, N.J: Prentice Hall, 1997.
[26] V. G. Veselago, "The electrodynamics of substances with simultaneously negative values of ϵ and μ," *Sov. Phys. Uspekhi*, vol. 10, no. 4, pp. 509–514, Apr. 1968, doi: 10.1070/PU1968v010n04ABEH003699.
[27] J. B. Pendry, A. J. Holden, D. J. Robbins, and W. J. Stewart, "Magnetism from conductors and enhanced nonlinear phenomena," *IEEE Trans. Microw. Theory Tech.*, vol. 47, no. 11, pp. 2075–2084, Nov. 1999, doi: 10.1109/22.798002.
[28] J. B. Pendry, A. J. Holden, D. J. Robbins, and W. J. Stewart, "Low frequency plasmons in thin-wire structures," *J. Phys. Condens. Matter*, vol. 10, no. 22, pp. 4785–4809, Jun. 1998, doi: 10.1088/0953-8984/10/22/007.
[29] J. B. Pendry, A. J. Holden, W. J. Stewart, and I. Youngs, "Extremely Low Frequency Plasmons in Metallic Mesostructures," *Phys. Rev. Lett.*, vol. 76, no. 25, pp. 4773–4776, Jun. 1996, doi: 10.1103/PhysRevLett.76.4773.
[30] T. Itoh, *Electromagnetic metamaterials: transmission line theory and microwave applications : the engineering approach*. Hoboken, N.J: John Wiley & Sons, 2010.

[31] D. R. Smith, W. J. Padilla, D. C. Vier, S. C. Nemat-Nasser, and S. Schultz, “Composite Medium with Simultaneously Negative Permeability and Permittivity,” *Phys. Rev. Lett.*, vol. 84, no. 18, pp. 4184–4187, May 2000, doi: 10.1103/PhysRevLett.84.4184.
[32] H. O. Moser, B. D. F. Casse, O. Wilhelmi, and B. T. Saw, “Terahertz Response of a Microfabricated Rod–Split-Ring-Resonator Electromagnetic Metamaterial,” *Phys. Rev. Lett.*, vol. 94, no. 6, p. 063901, Feb. 2005, doi: 10.1103/PhysRevLett.94.063901.
[33] T. F. Gundogdu *et al.*, “Experimental demonstration of negative magnetic permeability in the far-infrared frequency regime,” *Appl. Phys. Lett.*, vol. 89, no. 8, p. 084103, Aug. 2006, doi: 10.1063/1.2335955.
[34] W. J. Padilla, M. T. Aronsson, C. Highstrete, M. Lee, A. J. Taylor, and R. D. Averitt, “Novel electrically resonant terahertz metamaterials,” 2006, doi: 10.48550/ARXIV.COND-MAT/0605002.
[35] J. Pendry, “Metamaterials in the sunshine,” *Nat. Mater.*, vol. 5, no. 8, pp. 599–600, Aug. 2006, doi: 10.1038/nmat1697.
[36] F. Martín, J. Bonache, F. Falcone, M. Sorolla, and R. Marqués, “Split ring resonator-based left-handed coplanar waveguide,” *Appl. Phys. Lett.*, vol. 83, no. 22, pp. 4652–4654, Dec. 2003, doi: 10.1063/1.1631392.
[37] F. Falcone *et al.*, “Babinet Principle Applied to the Design of Metasurfaces and Metamaterials,” *Phys. Rev. Lett.*, vol. 93, no. 19, p. 197401, Nov. 2004, doi: 10.1103/PhysRevLett.93.197401.
[38] M. Gil, J. Bonache, and F. Martín, “Metamaterial filters: A review,” *Metamaterials*, vol. 2, no. 4, pp. 186–197, Dec. 2008, doi: 10.1016/j.metmat.2008.07.006.
[39] J. Naqui, M. Duran-Sindreu, and F. Martin, “Modeling Split-Ring Resonator (SRR) and Complementary Split-Ring Resonator (CSRR) Loaded Transmission Lines Exhibiting Cross-Polarization Effects,” *IEEE Antennas Wirel. Propag. Lett.*, vol. 12, pp. 178–181, 2013, doi: 10.1109/LAWP.2013.2245095.
[40] M. Gil, J. Bonache, I. Gil, J. García-García, and F. Martín, “On the transmission properties of left-handed microstrip lines implemented by complementary split rings resonators,” *Int. J. Numer. Model. Electron. Netw. Devices Fields*, vol. 19, no. 2, pp. 87–103, Mar. 2006, doi: 10.1002/jnm.601.
[41] J. Bonache *et al.*, “Super compact split ring resonators CPW band pass filters,” in *2004 IEEE MTT-S International Microwave Symposium Digest (IEEE Cat. No.04CH37535)*, Fort Worth, TX, USA: IEEE, 2004, pp. 1483–1486. doi: 10.1109/MWSYM.2004.1338854.
[42] G. E. Ponchak, “Coplanar Stripline Coupled to Planar Double Split-Ring Resonators for Bandstop Filters,” *IEEE Microw. Wirel. Compon. Lett.*, vol. 28, no. 12, pp. 1101–1103, Dec. 2018, doi: 10.1109/LMWC.2018.2875336.
[43] L. Smith, V. Shiran, W. Gomaa, and T. Darcie, “Characterization of a split-ring-resonator-loaded transmission line at terahertz frequencies,” *Opt. Express*, vol. 29, no. 15, p. 23282, Jul. 2021, doi: 10.1364/OE.432192.
[44] Z. Shaterian and M. Mrozowski, “A Multifunctional Microwave Filter/Sensor Component Using a Split Ring Resonator Loaded Transmission Line,” *IEEE Microw. Wirel. Technol. Lett.*, vol. 33, no. 2, pp. 220–223, Feb. 2023, doi: 10.1109/LMWC.2022.3208373.
[45] R. Marqués, F. Martín, and M. Sorolla, *Metamaterials with Negative Parameters: Theory, Design, and Microwave Applications*, 1st ed. Wiley, 2007. doi: 10.1002/9780470191736.
[46] S. A. Schelkunoff and H. T. Friis, *Antennas: Theory and Practice*. John Wiley & Sons, Inc, 1952.

[47] R. Marques, F. Mesa, J. Martel, and F. Medina, “Comparative analysis of edge- and broadside-coupled split ring resonators for metamaterial design - Theory and experiments,” *IEEE Trans. Antennas Propag.*, vol. 51, no. 10, pp. 2572–2581, Oct. 2003, doi: 10.1109/TAP.2003.817562.

[48] J. D. Baena *et al.*, “Equivalent-circuit models for split-ring resonators and complementary split-ring resonators coupled to planar transmission lines,” *IEEE Trans. Microw. Theory Tech.*, vol. 53, no. 4, pp. 1451–1461, Apr. 2005, doi: 10.1109/TMTT.2005.845211.

[49] R. Marqués, F. Medina, and R. Rafii-El-Idrissi, “Role of bianisotropy in negative permeability and left-handed metamaterials,” *Phys. Rev. B*, vol. 65, no. 14, p. 144440, Apr. 2002, doi: 10.1103/PhysRevB.65.144440.

[50] F. Martin, F. Falcone, J. Bonache, R. Marques, and M. Sorolla, “Miniaturized coplanar waveguide stop band filters based on multiple tuned split ring resonators,” *IEEE Microw. Wirel. Compon. Lett.*, vol. 13, no. 12, pp. 511–513, Dec. 2003, doi: 10.1109/LMWC.2003.819964.

[51] R. D. V. Ríos, S. Bikorimana, M. A. Ummy, R. Dorsinville, and S.-W. Seo, “A bow-tie photoconductive antenna using a low-temperature-grown GaAs thin-film on a silicon substrate for terahertz wave generation and detection,” *J. Opt.*, vol. 17, no. 12, p. 125802, Dec. 2015, doi: 10.1088/2040-8978/17/12/125802.

[52] P. U. Jepsen and B. M. Fischer, “Dynamic range in terahertz time-domain transmission and reflection spectroscopy,” *Opt. Lett.*, vol. 30, no. 1, p. 29, Jan. 2005, doi: 10.1364/OL.30.000029.

[53] O. Sydoruk, E. Tatartschuk, E. Shamonina, and L. Solymar, “Analytical formulation for the resonant frequency of split rings,” *J. Appl. Phys.*, vol. 105, no. 1, p. 014903, Jan. 2009, doi: 10.1063/1.3056052.

[54] K. Fertas, F. Ghanem, M. Challal, M. Ouahdi, F. Fertas, and R. Aksas, “Design and implementation of a novel tri-band bandstop filter based on hexagonal metamaterials split ring resonators,” in *2017 5th International Conference on Electrical Engineering - Boumerdes (ICEE-B)*, Boumerdes: IEEE, Oct. 2017, pp. 1–4. doi: 10.1109/ICEE-B.2017.8192101.

[55] S. J. Park and J. Cunningham, “Determination of Permittivity of Dielectric Analytes in the Terahertz Frequency Range Using Split Ring Resonator Elements Integrated with On-Chip Waveguide,” *Sensors*, vol. 20, no. 15, p. 4264, Jul. 2020, doi: 10.3390/s20154264.

[56] R. S. Parker-Jervis, S. J. Park, and J. E. Cunningham, “Tunable terahertz band-stop filter using strongly coupled split ring resonators integrated with on-chip waveguide,” *J. Appl. Phys.*, vol. 129, no. 5, p. 053101, Feb. 2021, doi: 10.1063/5.0040054.

[57] A. Singh *et al.*, “Up to 70 THz bandwidth from an implanted Ge photoconductive antenna excited by a femtosecond Er:fibre laser,” *Light Sci. Appl.*, vol. 9, no. 1, p. 30, Mar. 2020, doi: 10.1038/s41377-020-0265-4.

[58] S. L. Dexheimer, Ed., *Terahertz Spectroscopy: Principles and Applications*, 0 ed. CRC Press, 2017. doi: 10.1201/9781420007701.

[59] Perkin Elmer, “Low Level Optical Detection using Lock-in Amplifier Techniques.” Ametek Scientific Instruments (Signal Recovery), 2000. [Online]. Available: https://www.ameteksi.com/